OCEANOGRAPHY

Sea level and deep-sea temperature reconstructions suggest quasi-stable states and critical transitions over the past 40 million years

Eelco J. Rohling[1,2]*, Jimin Yu[1,3], David Heslop[1], Gavin L. Foster[2], Bradley Opdyke[1], Andrew P. Roberts[1]

Sea level and deep-sea temperature variations are key indicators of global climate changes. For continuous records over millions of years, deep-sea carbonate microfossil–based $\delta^{18}O$ (δ_c) records are indispensable because they reflect changes in both deep-sea temperature and seawater $\delta^{18}O$ (δ_w); the latter are related to ice volume and, thus, to sea level changes. Deep-sea temperature is usually resolved using elemental ratios in the same benthic microfossil shells used for δ_c, with linear scaling of residual δ_w to sea level changes. Uncertainties are large and the linear-scaling assumption remains untested. Here, we present a new process-based approach to assess relationships between changes in sea level, mean ice sheet $\delta^{18}O$, and both deep-sea δ_w and temperature and find distinct nonlinearity between sea level and δ_w changes. Application to δ_c records over the past 40 million years suggests that Earth's climate system has complex dynamical behavior, with threshold-like adjustments (critical transitions) that separate quasi-stable deep-sea temperature and ice-volume states.

INTRODUCTION

Ice sheets are a pivotal component of the climate system during icehouse periods. The current icehouse period started at the Eocene-Oligocene Transition (EOT), 34 million years (Ma) ago, when the Antarctic Ice Sheet (AIS) developed, followed by fluctuations in its volume with northern hemisphere glacial variations (*1*–*4*). Modern warming drives climate in the opposite direction, and improved estimates are needed for the associated long-term equilibrium sea level rise. This requires continuous sea level records that extend at least through the Middle Pliocene (about 3 to 3.3 Ma ago), the last time atmospheric CO_2 levels were similar to those of today (*4*–*7*). Records should preferably continue into more ancient times to ensure coherent results across the entire range of full glacial to completely ice-free climate states, which is essential for evaluating fundamental aspects such as climate-state dependencies of feedbacks, and climate tipping points.

Ice-volume changes have dominated sea level amplitudes since the EOT. Sea level per se, however, is only reasonably constrained in continuous records for the past 500 to 800 thousand years (ka), on the basis of records of marginal-sea isolation from the open ocean (*8*–*11*) and on statistical assessment across various methods (*12*). For more ancient times, deep-sea oxygen isotope records provide the dominant information source. We want to know seawater $\delta^{18}O$ (δ_w), but the data come in the form of carbonate microfossil $\delta^{18}O$ (δ_c) (*13*, *14*), which represents combined influences of δ_w and T_w. Analytically, T_w influences may be corrected using Mg/Ca data (*15*, *16*), but there are complications from oceanic Mg-concentration changes over time scales longer than a million years (*17*–*19*). Moreover, Mg/Ca thermometry has 1° to 1.5°C uncertainties (1σ) in cold deep-sea environments (*15*), while T_w signals commonly amount to only a few degrees, causing unfavorable signal-to-noise ratios (*16*). Even if T_w could be resolved without uncertainties, the resolved δ_w record would still need to be translated into ice-volume/sea level changes. This is commonly done by assuming a linear $\Delta\delta_w$:Δ_{SL} relationship, which is often "calibrated" to the Last Glacial Maximum (LGM)–to-modern δ_w gradient measured in marine sediment pore waters (*20*–*22*). However, these assumptions remain untested.

The ubiquitous reliance on linear $\Delta\delta_w$:Δ_{SL} approximations is unexpected given that, from first principles, the primary expectation should be that it is nonlinear. This is because ice sheets accumulate precipitation of increasingly negative $\delta^{18}O$ composition as they grow because of increasingly intense Rayleigh distillation and because different ice sheets begin to form and develop their $\delta^{18}O$ signature at different moments in time (and, hence, at different moments in global Δ_{SL} history). Thus, the global mean ice $\delta^{18}O$ will change with sea level, which imposes nonlinearity on the $\Delta\delta_w$:Δ_{SL} relationship. Here, we evaluate this issue quantitatively using a new approach based on straightforward representations of underlying process relationships and interdependencies, and we apply our mutually consistent reconstruction method for key parameters in paleoceanographic reconstructions. We start with a simplified analytical assessment of the $\Delta\delta_w$:Δ_{SL} relationship to illustrate its fundamental nature and sensitivity to key assumptions and uncertainties. Thereafter, we present applied assessments that use published sea level records to determine mutually consistent variations in Δ_{SL}, ice sheet volumes (V_{ice}), δ_{ice}, T_w, and δ_w, culminating in a detailed assessment over the past 40 Ma. Sensitivity tests and a range of independent validation criteria are used to assess the robustness of results, and key avenues for further improvements are highlighted.

Our mutually consistent, process-based framework for Δ_{SL}, V_{ice}, δ_{ice}, T_w, and δ_w permits complete system validation using multiple parameters rather than only one or two as in traditional approaches. We obtain new records for these parameters, which are of fundamental interest in (paleo)climate science, and that are independently cross-validated over at least the past 22 Ma. This approach provides a testable way to understand relationships among measurable parameters and underlying processes of interest in understanding climate change.

[1]Research School of Earth Sciences, Australian National University, Canberra, ACT 2601, Australia. [2]School of Ocean and Earth Science, University of Southampton, National Oceanography Centre, Southampton SO14 3ZH, UK. [3]Pilot National Laboratory for Marine Science and Technology (Qingdao), Qingdao 266237, China.
*Corresponding author. Email: eelco.rohling@anu.edu.au

RESULTS

Relationship between precipitation $\delta^{18}O$ and ice sheet volume

The volume (V) of ice sheets is a key determinant in the $\delta^{18}O$ of their newly accumulating precipitation (δ_p). Past work has related low δ_p, reflected in the $\delta^{18}O$ of accumulated ice (δ_{ice}), to intense Rayleigh distillation of atmospheric vapor through successive vapor saturation/condensation cycles with decreasing temperature along vapor pathways from evaporative sources to condensation/precipitation sites [e.g., (*23*, *24*), review in (*25*)]. Rayleigh distillation intensifies with cooling during atmospheric vapor transport from oceanic evaporation sites to high latitudes, from coastal regions to cold (winter) continental interiors, and from lower to higher altitudes. This is because vapor saturation drops nonlinearly with decreasing temperature (Clausius-Clapeyron relationship), while Rayleigh distillation follows a natural logarithmic relationship to more negative values with reduction in the fraction of remaining atmospheric vapor (*25*). As a result, relatively low-altitude seasonal snow over ground or small snow patches has much less negative δ_p than snow falling at the center of a large, high-altitude continental ice sheet. While this is an idealized representation and there are additional controlling factors (*26*), we address this both here with a sensitivity test (below) and in our final outlook for further method development.

Seasonal snow δ_p typically reaches −10 to −20‰ [e.g., (*27*–*29*)]. Values become more negative with distance from the coast and with increasing altitude; for example, a trans-Alaskan continental gradient exists of −8.3‰/1000 km from the coast, with a superimposed orographic $\delta^{18}O$ decrease of −6.8‰/km of altitude (*28*). As regional ice-albedo effects combine with high altitude, intense cooling in cold mountain regions with permanent ice (glaciers and ice caps) cause δ_p to typically reach −25‰ or even −30‰, with lowest values recorded in winter [e.g., (*30*–*33*)]. Hence, a sharp initial δ_p drop is apparent between initial snow and sustained precipitation over nascent high-altitude, permanent ice bodies. Eventually, δ_p can reach −60‰ or lower in the coldest, most isolated locations of the intensely cold hearts of major, kilometers-high continental ice sheets, such as the Antarctic interior (*34*). Rayleigh distillation between evaporative sources and precipitation sites was less extreme for the North American Laurentide Ice Sheet (LIS) and the Eurasian Ice Sheet (EIS) during ice ages because of their positions in lower ("warmer") latitudes closer to relatively warm oceanic moisture sources. For example, five isotope-enabled global climate circulation models indicate that the LIS reached a minimum LGM δ_p of about −38‰ (*35*).

We represent δ_p changes over ice sheets as a generic function of V, starting with an initial snow δ_p = −15‰ that drops rapidly with initial ice sheet volume buildup, followed by an exponential change with V toward very negative values over large ice sheets (Methods, Eq. 1, and fig. S1). We use two sets of equation constants to account for more intense Rayleigh distillation over high-latitude "cold" ice sheets than over lower-latitude warmer ice sheets. In our analytical assessment, sensitivity test 1 uses a different relationship that is simply linear (Methods and Eq. 2)—albeit physically implausible—to evaluate the importance of the selected function shape for the conclusions, given that our idealized representation may overlook additional controls on δ_p (*26*).

Analytical assessment

We use simple growth descriptions for the AIS as a single entity that represents both the East and West AIS, Greenland Ice Sheet (GrIS), EIS, and LIS, where the latter refers collectively to the LIS and Cascadian Ice Sheet. V_{AIS} today is 57.8 m sea level equivalent (m_{seq}) and V_{GrIS} is 7.3 m_{seq} (*36*) so that Δ_{SL} = +65.1 m in an ice-free state. In this analytical assessment, we assume that AIS and GrIS grow proportionally between Δ_{SL} = +65.1 and 0 m. Growth of continental ice sheets (i.e., glaciation) relative to the present caused negative Δ_{SL}, mainly due to growth of LIS and EIS (which do not exist today) along with slight AIS and GrIS expansions. Common approximations for the LGM are that Δ_{SL} was roughly −125 m because LIS had reached of the order of 70 m_{seq} and EIS about half that, while AIS grew by roughly 15 m_{seq} [see overview in (*37*)]. Here, we simply assume that GrIS grew another ~5 m_{seq}, which may be an overestimate, but this does not appreciably affect results, especially because less GrIS growth would need to be compensated by more growth in other ice sheets to keep the sea level budget closed. For different glacial maxima, size dominance may have alternated between LIS and EIS [see overview in (*37*)], but this does not affect results either because both are similar types of "warm" ice sheet in our calculations. We assume initially that all expansions were linearly proportional to Δ_{SL}. This gives individual ice sheet V variations relative to Δ_{SL} (Fig. 1A) and their sum V_{tot} (Fig. 1C).

The schematic ice sheet V variations can now be combined with the chosen relationship between δ_p and ice sheet volume (Methods and Eq. 1 or 2) to determine δ_p developments for each ice sheet (Fig. 1B). We assume that all ice sheets are equilibrated with δ_p; that is, the mass-weighted mean δ_{ice} of each ice sheet (indicated by $\overline{\delta_{ice}}$) is assumed to equal δ_p (this simple instantaneous equilibration assumption is addressed in detail below in our applied assessments). Next, we calculate the mass-weighted mean global δ_{ice} value for all accumulated ice (i.e., δ_{ice}*; Methods and Eq. 3). Last, relative δ_w changes (i.e., $\Delta\delta_w$) are determined using an ice-to-water density ratio of 0.9, a value for global ocean volume (V_{oc}) of 3700 m_{seq}, and $\Delta_{SL} = -\{(V_{AIS} - 57.8) + (V_{GrIS} - 7.3) + V_{LIS} + V_{EIS}\}$ (Methods and Eq. 4). In sensitivity test 2, the AIS is set to grow nonlinearly during glaciation (Δ_{SL} < 0 m), giving it a somewhat increased expansion rate during final glaciation stages. This test investigates the possible influences of a hypothetically enhanced AIS contribution to a marked final sea level drop (*38*) that coincided roughly with AIS expansion to its maximum LGM extent (*39*); the overall sea level budget is kept unchanged by setting LIS to grow nonlinearly in the opposite sense (Fig. 1A). We find (below) that this nonlinearity is too small to significantly affect the outcome of our analysis and the same holds if we invert the nonlinearity between AIS and LIS [the condition suggested in (*38*)].

The main case and both sensitivity tests reveal pronounced nonlinearity between Δ_{SL} and δ_{ice}* and, thus, between Δ_{SL} and $\Delta\delta_w$ (Fig. 1, C and D). Similar $\Delta\delta_w$:Δ_{SL} relationships for all three cases indicate that the pattern is robust with respect to the choice of V:δ_p relationship, details of ice sheet growth histories, or both (Fig. 1D). This is because the nonlinearity arises principally from addition of two much less negative ice sheets at Δ_{SL} < 0 (which increases δ_{ice}*) to the virtually fully formed and isotopically very negative AIS. Thus, the nonlinearity is a robust, unavoidable consequence of different glaciation thresholds for different ice sheets at different latitudes. Even if the same δ_p function were used for LIS and EIS as for AIS and GrIS, considerable nonlinearity would remain because LIS and EIS in their initial stages (up to 50 m_{seq}) have more positive δ_p than AIS.

Applied assessments

Here, we use published sea level records to determine mutually consistent variations in ice sheet volumes, δ_{ice}, T_w, and δ_w. A flow diagram

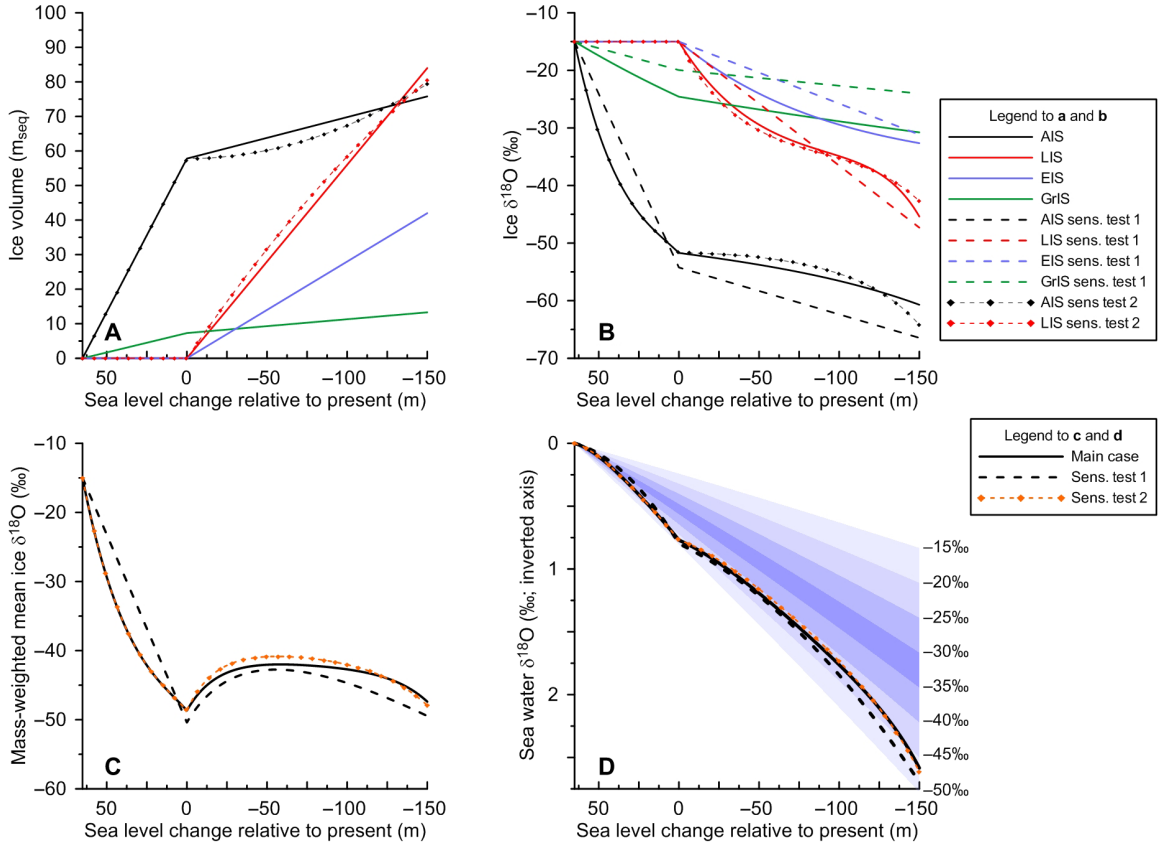

Fig. 1. Results of the analytical assessment. (**A**) Volume of each ice sheet relative to total sea level change caused by all ice sheet changes. (**B**) Ice $\delta^{18}O$ for each ice sheet. (**C**) Global volume- (or mass-) weighted mean ice $\delta^{18}O$ for all accumulated ice (note that in terms of proportions, mass weighting and volume weighting are equivalent here). (**D**) Changes in seawater $\delta^{18}O$ relative to sea level change. Solid lines indicate the main case (Methods and Eq. 1), dashed lines are for sensitivity test 1 (Methods and Eq. 2), and dotted lines are for sensitivity test 2. Shaded intervals in (D) indicate linear $\Delta\delta_w$:Δ_{SL} relationships that would occur if global mean ice $\delta^{18}O$ were constant at the indicated values. The overall steepness of lines in (D) is addressed in our applied assessments.

for the entire method is presented in fig. S2. From this workflow, the initial step of regression-based conversion of δ_c changes into Δ_{SL} is omitted when results are produced for published sea level records for comparison with δ_c-based results. Our method uses a straightforward model for growth of generic ice sheets with circular plano-convex lens shapes, axially symmetric parabolic profiles (*40*), and a constant height:radius aspect ratio $\varepsilon = 2 \times 10^{-3}$ (roughly the mean aspect ratio of the modern AIS). Unless specified otherwise, global ice-volume variations are determined in terms of sea level–equivalent changes, accounting for the density difference between ice and water. Model ice sheets retain their shape characteristics throughout, while sea level change between individual time steps is used to determine global net ice-volume growth or loss, which is partitioned over the different ice sheets as described in Methods (Eqs. 5 to 11). Thermosteric sea level changes are not considered.

The model contains one large and one smaller ice sheet that both disappear at the present-day sea level; these approximate LIS and EIS. It is irrelevant which of the two grows larger and which stays smaller, as all model ice sheets are generic, without geographic attribution, and both LIS and EIS approximations are taken to be warmer ice sheets for Rayleigh distillation (Methods and Eq. 1). The model approximates GrIS with $V_{GrIS} = 7.3\ m_{seq}$ at $\Delta_{SL} = 0$ m and AIS with $V_{AIS} = 57.8\ m_{seq}$ at $\Delta_{SL} = 0$ m (*36*). Ice-volume changes are driven in accordance with the applied sea level records and are attributed to the various ice sheets as discussed in Methods (Eqs. 5 to 11). δ_p changes over the ice sheets are calculated as in the main case of the analytical assessment above, using Methods and Eq. 1.

At this stage, we abandon the simplistic assumption that $\overline{\delta_{ice}}$ for each ice sheet is instantaneously similar to δ_p and instead calculate its time evolution (Methods and Eqs. 12 to 14). The initial assumption needed to be abandoned because δ_p instantaneously tracks ice sheet dimension changes, whereas it takes time for $\overline{\delta_{ice}}$ to equilibrate with changing conditions. Internal ice sheet properties reflect surface accumulation, downward and outward ice flow (ice dynamics), and ice loss through melting and calving. Thus, ice sheets contain contiguous ancient ice sequences within their interiors; in GrIS, this dates back to at least 125 ka ago (*41*) and in AIS to at least 800 ka ago (*42*, *43*). AIS has been at (almost) its modern size long enough that even ancient ice formed from precipitation with δ_p close to present values, but in short-lived ice sheets, especially LIS and EIS, a noticeable lag is expected between ice-volume buildup and full $\overline{\delta_{ice}}$ equilibration to the volume change. This lag is roughly 17 to 20 ka/m_{seq}, based on modern maximum ice ages and the GrIS and AIS sizes, but may be ice sheet size and, thus, time dependent. Given this uncertainty, we refrain from applying a standard lag function and instead resolve $\overline{\delta_{ice}}$ evolution directly per time step (Methods and Eq. 14).

Here, $\overline{\delta_{ice}}_j$ is calculated at time step j using ice sheet volume and $\overline{\delta_{ice}}_{j-1}$ of preceding time step $j-1$, and both gross mass accumulation with more negative δ_{ice} (determined from the δ_p relationship above) and gross mass loss with δ_{ice} that is (before achieving isotopic equilibration) less negative between time steps $j-1$ and j. We use $\overline{\delta_{ice}}_{j-1}$ for the latter term, along with a gross mass loss term that is determined by gross accumulation minus net accumulation/loss (where loss is negative). Net accumulation/loss is obtained from sea level variations, and gross accumulation (a_{grs}) is calculated in an ice sheet surface-area–dependent manner directly proportional to modern global annual a_{grs} of ~0.008 m_{seq} [following rates in (*44*, *45*)] for a global ice volume of 65.1 m_{seq}.

Annual a_{grs} is ~0.01% relative to ice volume and is set to change proportionally with ice sheet size, so the model ice sheets have isotopic equilibration time scales of the order of 10^4 years. This time scale is especially relevant for LIS and EIS, which existed only during glacial stages with life spans of order 10^4 to at most 10^5 years, and that typically reached maximum sizes only millennia before rapid glacial terminations. As a result, LIS and EIS were continually playing catch-up in terms of isotopic equilibration to their marked size changes. In the Late Pleistocene, the more permanent AIS (and, to a lesser extent, also GrIS) largely maintained conditions close to isotopic steady state. This did not hold during the Pliocene and older times, when considerable sea level changes well above 0 m imply major V_{GrIS} and V_{AIS} changes.

On the basis of ice-volume change, which is equated to sea level change (Δ_{SL}), and the combination of all ice sheet V and $\overline{\delta_{ice}}$ values, we can now determine $\Delta\delta_w$ (Methods and Eq. 15) and, thus, the Δ_{SL}:$\Delta\delta_w$ relationship. Each ice sheet's contribution to $\Delta\delta_w$ depends on its V and $\overline{\delta_{ice}}$, so that the aforementioned time lag between volumetric changes and $\overline{\delta_{ice}}$ equilibration holds considerable potential to influence Δ_{SL}:$\Delta\delta_w$ nonlinearities.

Subtraction of the calculated $\Delta\delta_w$ record from δ_c [e.g., (*13*, *14*)] resolves the δ_c component that relates to T_w changes by –0.25‰ $°C^{-1}$ (*15*, *16*). These T_w changes can then be compared with Mg/Ca-based T_w reconstructions to assess model-based V_{ice}, δ_{ice}, T_w, and δ_w variations. However, chronological offsets between model-input Δ_{SL} and calculated δ_w on the one hand, and δ_c on the other hand, may cause large spurious T_w signals that obfuscate validation. Hence, closely synchronized records, or—better still—signals coregistered in a single sample set, are essential. We, therefore, only use T_w validation when this condition is met.

We apply our method to several input Δ_{SL} records, each with different underpinning assumptions and uncertainties (Figs. 2 and 3A). We use a 550-ka Red Sea marginal-basin residence-time record multiplied by 1.1 to approximate global mean sea level changes (*8*–*11*), an 800-ka multimethod sea level stack (*12*), and a 5.3-Ma Mediterranean marginal-basin record that is known to give pre–1.2 Ma values that are biased too high (Fig. 2B) (*46*). These Δ_{SL} reconstructions are not entirely independent of each other; notably, the Red Sea (*8*–*11*) and Mediterranean (*46*) records each contribute ~$^1/_7$ of the multimethod sea level stack (table S1) (*12*). This does not affect our approach because results from these Δ_{SL} reconstructions are shown only for mutual comparison, to illustrate that our method is broadly applicable and not specific to any one realization.

To allow application of our method to more ancient times, we use two Δ_{SL} records from deep-sea benthic foraminiferal δ_c records. These δ_c records are a 5.3-Ma stack (*13*) and the youngest 40 Ma of a 67-Ma global megasplice (Figs. 2, B and C, 3A, and 4A) (*14*). Δ_{SL} fluctuations are inferred from these δ_c records using a lag-optimized quadratic regression between the 800-ka multimethod Δ_{SL} stack and δ_c (*12*). This regression was originally constrained up to about Δ_{SL} = +15 m and, here, needs extrapolation to ice-free conditions. Therefore, we reevaluate the quadratic regression while constraining it to peak at Δ_{SL} = +65.1 m.

Two other regressions are used as sensitivity tests. One represents the upper 95% confidence limit of the constrained quadratic regression. The other represents an unconstrained quadratic regression through the same dataset (see Methods and fig. S3). Results for the latter are shown in orange in Figs. 3A and 4A but are virtually indistinguishable from the main case (black lines) over the Plio-Pleistocene (Fig. 3) and top out at ~56 m in more ancient times so that this record suggests consistent ice presence before the EOT at 34 Ma ago (Fig. 4A). In view of reports that some ice may have existed in Antarctica before the EOT [e.g., (*1*, *47*)], we cannot exclude the orange estimates. However, given that these estimates retain significant ice volume before the EOT, we consider them to be unlikely minimum sea level estimates. The main constrained regression (black) provides the lowest sea level estimates that are still consistent with an ice-free pre-EOT state and limited Middle Miocene ice conditions—these represent our best estimates. Conversion regressions from δ_c to Δ_{SL} that are steeper than the upper 95% confidence limit of our forced regression (pink in Figs. 3A and 4A) lead to unrealistic, long-lasting, ice-free conditions through the Middle Miocene; we, thus, consider the pink line as an upper sea level estimate. Our approach differs from previous modeling that deconvolved δ_c into Δ_{SL}, and T_w components, where the latter are assumed to be northern hemisphere–driven (*4*). We do not use that Δ_{SL} record as input because its origin in δ_c would risk introducing circularity; we use it for comparison only.

Modeled time series for V_{ice} and $\overline{\delta_{ice}}$ based on the various Δ_{SL} records are presented in figs. S4 to S6. Although differences between the input Δ_{SL} records reverberate through the solutions in an absolute sense, the choice of Δ_{SL} record, as long as it has a realistic amplitude and timing structure (relative to previous sea level records and ice volumes of the ice sheets concerned), does not affect relative relationships among V_{ice}, $\overline{\delta_{ice}}$, $\Delta\delta_w$, and T_w because those relationships arise from the modeled processes rather than from input values. Therefore, plotting of parameters from individual model runs provides substantial information on time-dependent behavior among parameters, across the full range of sea level values covered by the input Δ_{SL} records (Figs. 2 to 6). All variables of interest are mutually consistent so that validation of one typically implies validation of the others (Figs. 3, A and C to E, and 4, A to D). Before evaluating validation against observations, we make two initial observations.

First, slow isotopic equilibration to volumetric changes causes marked V versus $\overline{\delta_{ice}}$ hysteresis for each ice sheet (Fig. 5). This arises from slow (lagging) $\overline{\delta_{ice}}$ adjustments to growing ice sheets until the glacial maxima when the most negative $\overline{\delta_{ice}}$ was achieved and subsequent rapid and large-amplitude deglacial net ice losses (Fig. 5). At each (partial) deglaciation, values shoot almost horizontally to the left in the hysteresis diagrams, leading into a jump that can be almost vertical—especially in the most marked cases of complete LIS and EIS deglaciation—as incipient glaciation starts again with new snow at δ_p = −15‰. The AIS only undergoes these fluctuations in the hysteresis diagrams when it experiences substantial volume reductions (i.e., at Δ_{SL} > 0 m, during the Pliocene and more ancient times).

Second, the $\Delta\delta_w$:Δ_{SL} relationships obtained from paleorecords (Fig. 6) clearly follow the same general $\Delta\delta_w$:Δ_{SL} nonlinearity found

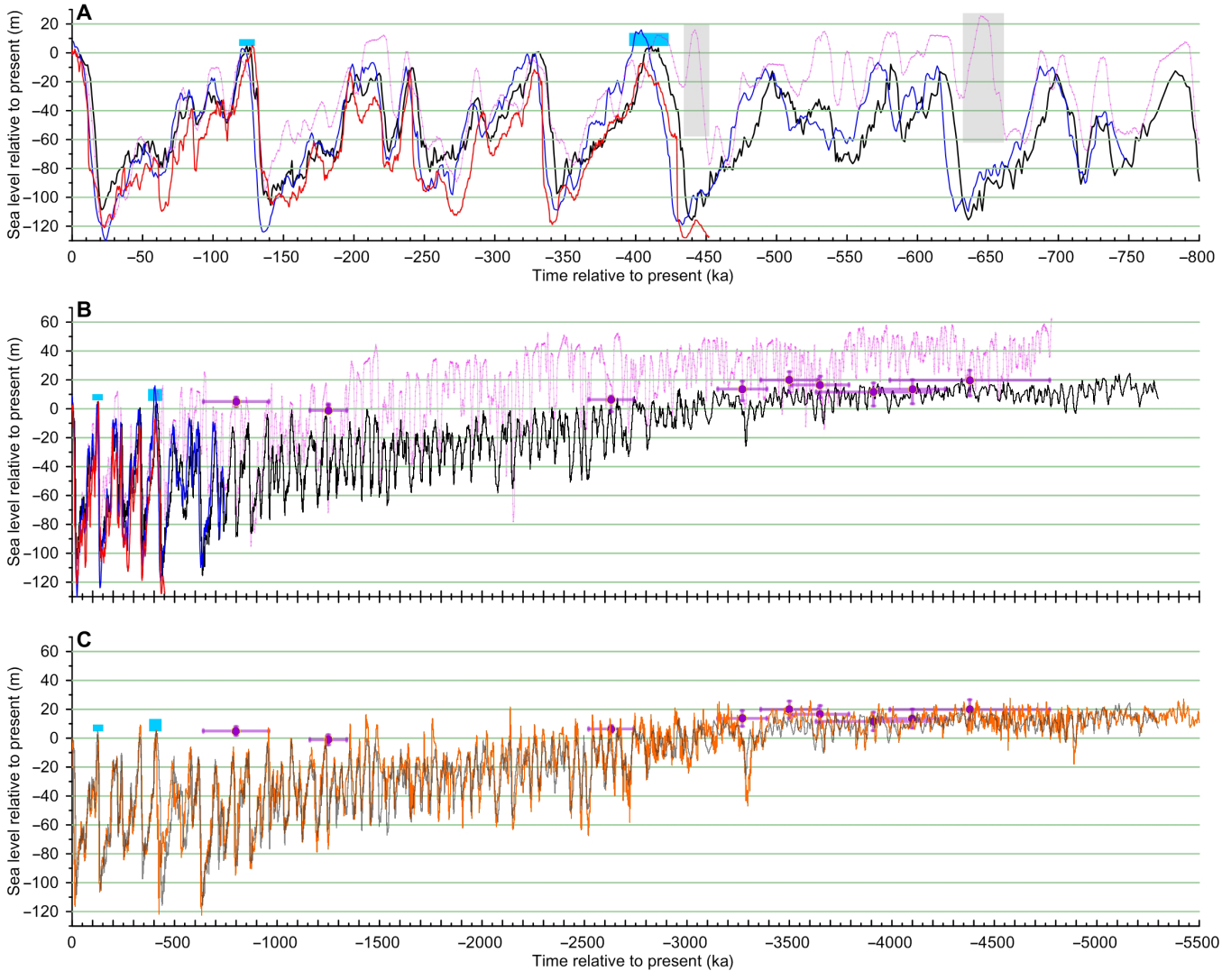

Fig. 2. Sea level records used in this study. (**A** and **B**) Comparison between the sea level solutions based on the Red Sea record [red; (*8*–*11*)], the statistical sea level record [blue; (*12*)], the Mediterranean Sea record that is known to be biased high before 1.2 Ma ago [magenta; (*46*)], the benthic δ_c stack-based sea level record [black; (*13*)], and western Mediterranean cave-based benchmarks [purple; (*49*, *50*), where the youngest three points come from the more recent publication] [(A) is an expanded image of the last 800,000 years from (B)]. The same age scale is used in (B) and (C). (**C**) Comparison between the benthic δ_c stack-based sea level record [black; (*13*)] and the benthic δ_c megasplice-based sea level record [orange; (*14*)] (both based on the main case regression in fig. S3) and western Mediterranean cave-based benchmarks [purple; as in (B)]. The δ_c megasplice-based record has greater amplitudes, which may suggest that some amplitude reduction/smoothing has resulted from δ_c stack calculation. All chronologies are as presented in the original studies. In all three panels, the light blue rectangles indicate multiproxy best-fit sea level estimates for MIS 5e and 11; these rectangles are to scale only for sea level, not for age (*48*). Our two benthic δ_c-based sea level records reach the lower regions of these multiproxy best-fit interglacial sea level estimates, which likely results from failure of the benthic δ_c-based sea level records to fully resolve millennial-scale features, which are important for capturing range extremes (*51*).

in our analytical assessment (Fig. 1D). This substantially affects the way $\Delta\delta_w$ is reconstructed through time relative to traditional approaches that assume a linear $\Delta\delta_w$:Δ_{SL} relationship (fig. S7). By resolving the mass-weighted mean global δ_{ice} value for all accumulated ice (δ_{ice}*) at every time step in accordance with evolving characteristics of the ice sheets, our reconstruction allows $\Delta\delta_w$ to shift seamlessly across lines obtained from $\Delta\delta_w$:Δ_{SL} relationships based on different δ_{ice}* values. This removes the need to assume which δ_{ice}* value applies at specific times and how and when shifts between these values occurred. Our method thus provides a major step toward the necessity—specified in the most recent long-term sea level assessment—that "changes in the [… $\Delta\delta_w$:Δ_{SL} …] calibration with evolution of ice-sheet size should be modeled" (*3*). We note that the shape of the $\Delta\delta_w$:Δ_{SL} nonlinearity identified from our modeling remains robust even when combining data points from model runs for all Δ_{SL} records, with all of their different underpinning assumptions and uncertainties (Fig. 6D). This indicates that the shape is largely insensitive to the distinct V:$\overline{\delta_{ice}}$ hysteresis for individual ice sheets, which was omitted from our analytical assessment. There are impacts only on the overall slope of the lines and data distributions around the regression. However, such robustness does not imply that the model approximates reality well; it merely reflects internal model consistency. Validation against

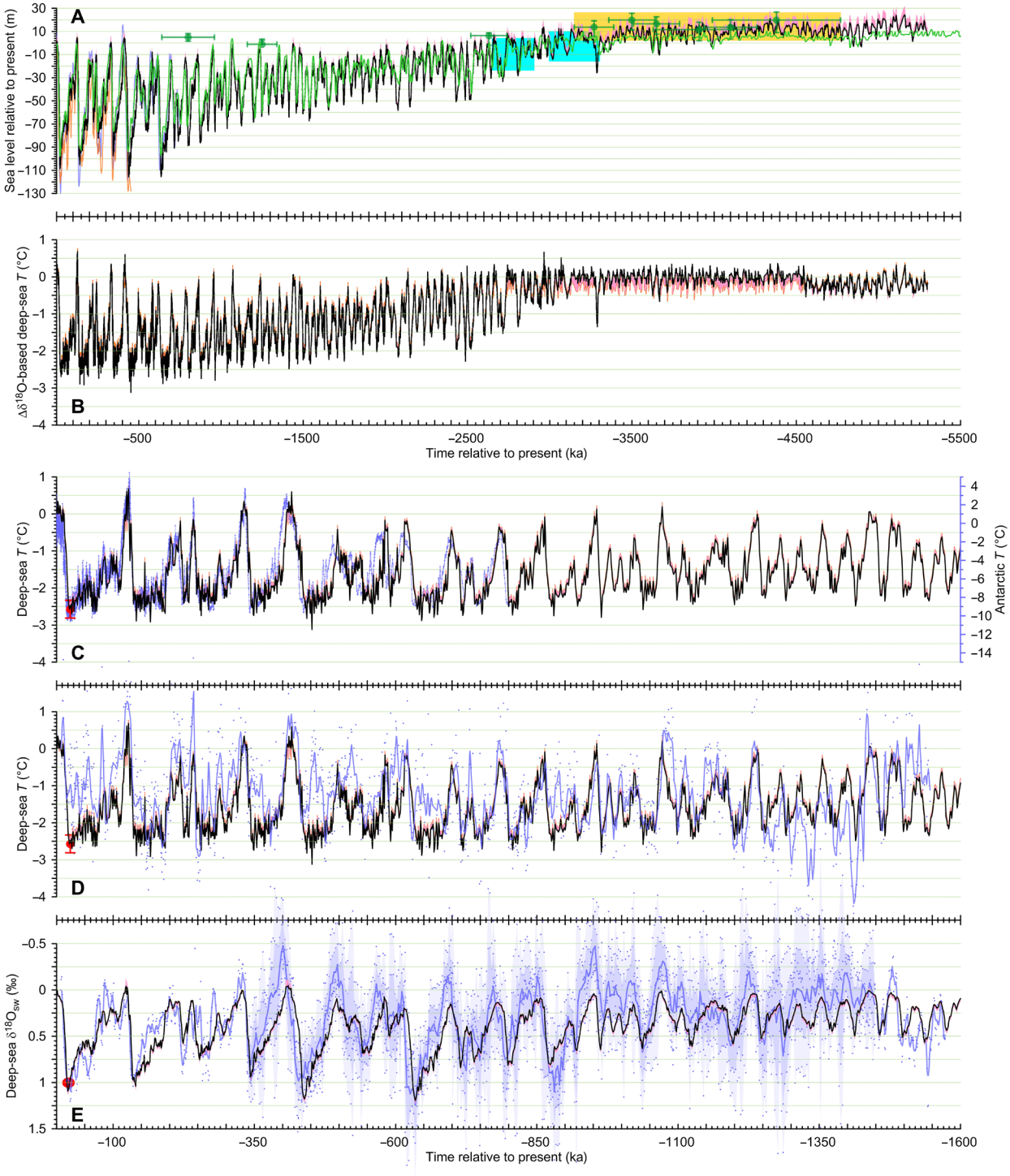

Fig. 3. Comparison of our Δ_{SL}, T_w, and δ_w with other observations. (**A**) Sea level change from the sea level stack [(*12*), blue]; from the Red Sea record, × 1.1 to approximate global mean sea level variations [(*11*), orange]; from model-based δ_c deconvolution [(*4*), green]; and from lag-optimized, quadratic regression between (*13*) and (*12*) (fig. S3) forced to peak at Δ_{SL} = 65.1 m (black), and from the regression's upper 95% confidence limit (pink). Cyan boxes indicate maximum amplitude envelopes of New Zealand relative sea level fluctuations (*52*), vertically positioned for comparison. Green dots are western Mediterranean benchmarks (*49*, *50*), with highlighted Middle Pliocene range (yellow box). (**B**) T_w changes derived using δ_c and δ_w, where δ_w is calculated from Δ_{SL} [this study; black and pink using Δ_{SL} in (A); orange using Δ_{SL} from the unconstrained regression; fig. S3]. (C) to (E) all on the age scale of (E). (**C**) Last 1.6 Ma of (B) versus Antarctic (EDC) temperature on its independent chronology (*54*). Red dot represents a noble gas–based estimate of LGM global ocean cooling, plotted against the T_w axis (*57*). (**D**) As (C) but versus Mg/Ca-based T_w [(*16*), blue, individual data and 4-ka Gaussian smoothing]. (**E**) As (D), but for δ_w. We show ODP Site 1123 (*16*) alone at 0 to 0.35 and 1.45 to 1.6 Ma ago and a three-record δ_w stack including ODP 1123 for 0.35 to 1.45 Ma ago, with 1× and 2× bootstrap errors (*58*). Red dot indicates LGM sediment pore-water–based δ_w (*20*–*22*).

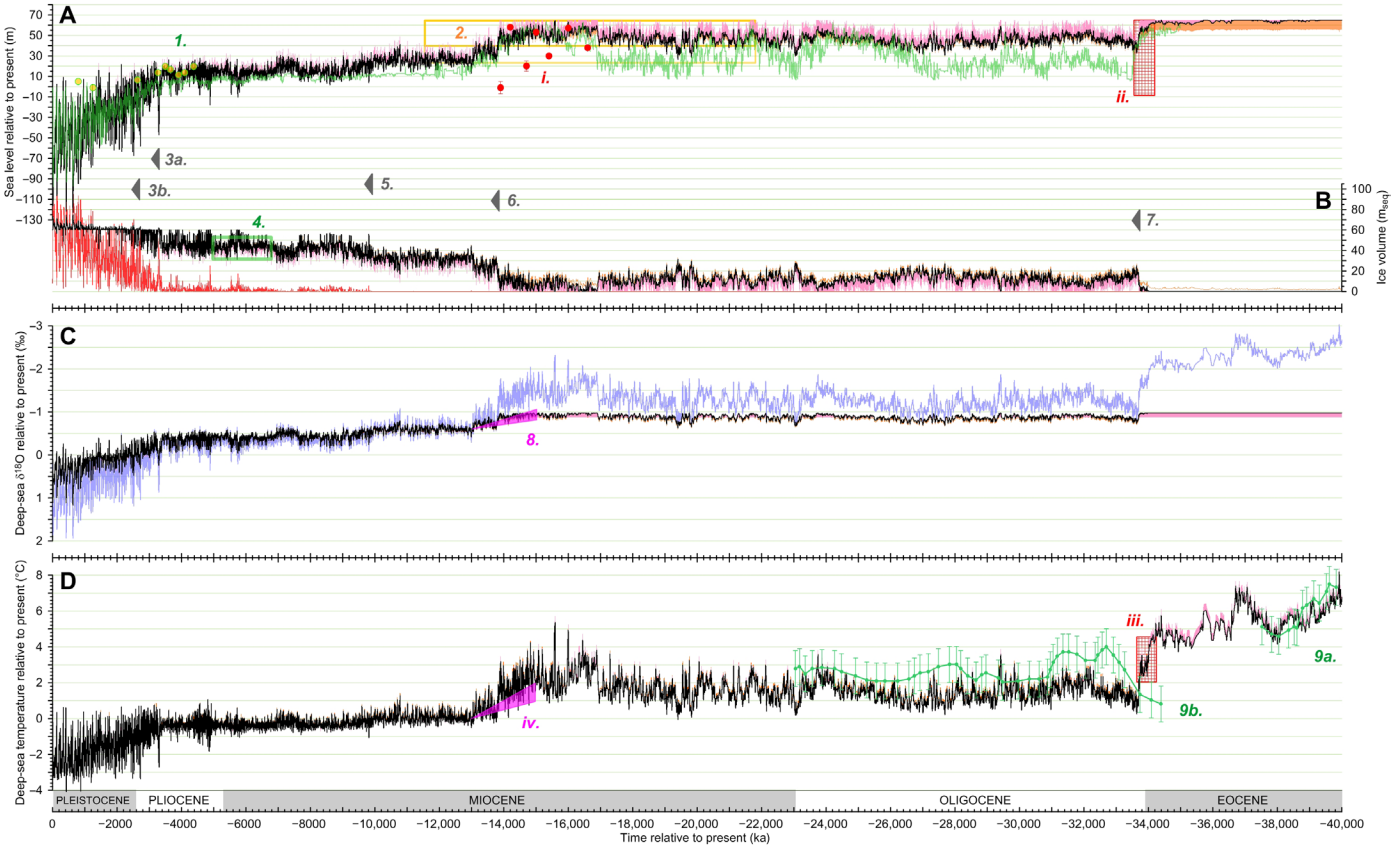

Fig. 4. Validations for our 40-Ma records. (**A**) Sea level variations from δ_c (*14*) based on our main-case regression (black), upper 95% confidence bound (pink), and unconstrained quadratic regression (orange) (fig. S3); and previous model-based δ_c deconvolution [(*4*), green]. (**B**) Our results for AIS (black, pink, and orange as above) and northern ice volume (LIS + EIS + GrIS; red, only for the main regression for clarity). (**C**) Model-derived δ_w based on our Δ_{SL} in (A) (black, pink, and orange) versus δ_c [(*14*), lilac]. (**D**) T_w changes based on δ_c residuals in(C) (black, pink, and orange). Regular italic numbers indicate positive validations: *1*, western Mediterranean benchmarks (*49*, *50*); *2*, best- and maximum-amplitude sea level ranges (*53*); *3a* and *3b*, first major iceberg calving in Nordic Seas (*59*) and LIS calving onset (*60*), respectively; *4*, AIS-volume variability range (*61*); *5*, onset partial/ephemeral northern ice (*1*); *6*, end of last intermittently ice-free period (*3*); *7*, AIS glaciation onset (*1*, *3*, *4*, *64*, *66*–*70*); *8*, MMCT δ_w change of 0.35 ± 0.12‰ (*62*); *9a* and *9b*, loess fit through Mg/Ca T_w with 95% confidence bounds; at 34.5 to 37.5 Ma ago, data were questioned (*67*). Roman numerals indicate discrepancies: *i*, amplitudes of sea level change in North West Australia (*63*); *ii*, EOT sea level drop of 70 to 80 m (*64*) versus ~30 m in this study (Discussion); *iii*, 2.5°C EOT cooling (*66*) versus 3.5°C cooling here (Discussion); *iv*, MMCT cooling of 1.5° ± 0.5°C (*62*) versus 2.5° ± 0.5°C here.

independent observations is needed to assess whether the calculated records are realistic (Discussion and Figs. 3, A, C, and D, and 4, A to D).

DISCUSSION

Validation of results

Clear linear progression in our method illustrates an absence of circularities; fundamental assumptions exist only at two stages (fig. S2). One assumption concerns regression-based derivation of Δ_{SL} from δ_c (fig. S3). Yet, sensitivity tests with realistically different regressions (fig. S3) indicate that our δ_c-based Δ_{SL} record is robust within about 10 m (total range; Figs. 3A and 4A). Diverse validations of the mutually consistent Δ_{SL}, $\overline{\delta_{ice}}$, δ_w, and T_w records support this robustness (below). The other assumption concerns the chosen δ_p versus ice-volume relationships. Sensitivity tests with alternative linear relationships indicate that our conclusions are robust regardless of the relationship shape (Fig. 1, C and D).

Below, we compare our reconstructions with independent observations. A first validation against observations is that even at the largest LIS volumes, LIS $\overline{\delta_{ice}}$ barely reached −35‰ (Fig. 5), while values integrated over 100-ka glacial cycles within the past 500 ka are consistently between about −25 and −35‰ (fig. S5). Groundwaters in North America that reflect subglacial or preglacial recharge typically reach −26‰, with a possible −28‰ end member, while ground ice in Yukon and the Barnes Ice Cap, Nunavut (both in Canada) has values of −29 to −35‰ (*35*). These values agree well with our LIS $\overline{\delta_{ice}}$ simulations.

Next, we observe reasonable agreement between our new δ_c regression–based Δ_{SL} and independent multiproxy sea level reconstructions for interglacial Marine Isotope Stages (MIS) 5e and 11 (*48*), the Red Sea sea level record (*11*), and Middle Pliocene sea level benchmarks (Figs. 2, A and C, and 3A) (*49*, *50*). The δ_c records that underpin our regression-based Δ_{SL} do not fully resolve millennial-scale features, so our new (δ_c regression–based) Δ_{SL} records are likely to miss short-term extremes of several-meters amplitude that can be important in interglacials like MIS 5e and 11 [e.g., (*51*)]. Compared with the Red Sea record (*11*), our new Δ_{SL} records agree much better with the multiproxy assessment for MIS 11 (*48*), a further indication

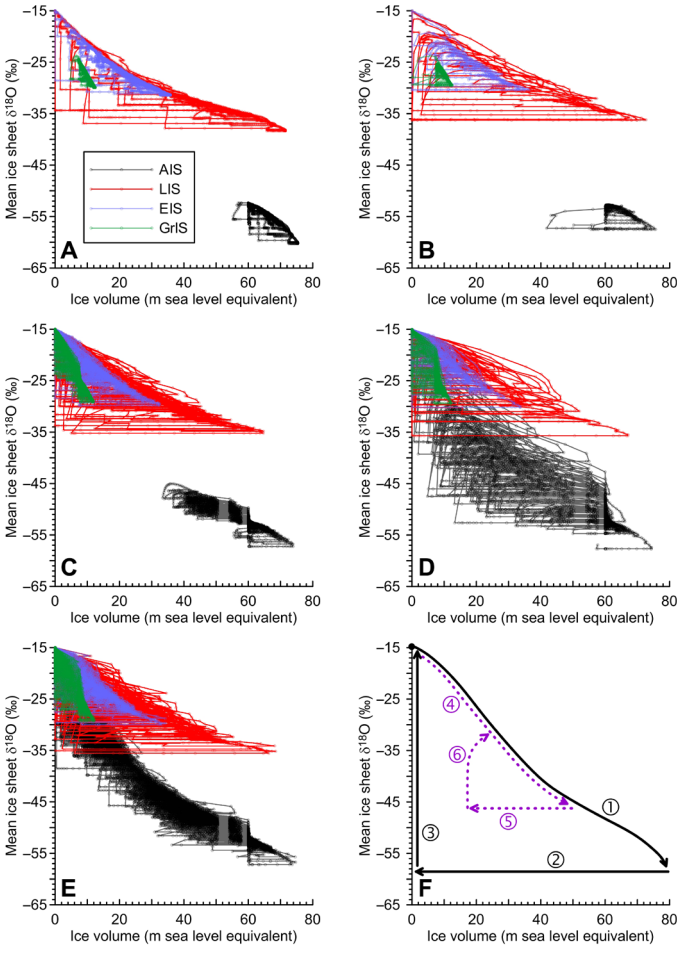

Fig. 5. Diagrams of $\overline{\delta_{ice}}$ relative to ice sheet volume for individual ice sheets for the five main model runs investigated in this study. (**A**) Sea level record based on the Red Sea method (*8*–*11*), (**B**) sea level stack (*12*), (**C**) benthic δ_c stack-based sea level record (main regression in fig. S3) (*13*), (**D**) sea level record from the Mediterranean Sea method (*46*), and (**E**) youngest 40 Ma of the benthic δ_c megasplice-based record (main regression in fig. S3) (*14*). The less complete V_{ice}:$\overline{\delta_{ice}}$ representations are for shorter records that do not cover the full bipolar ice sheet response range; the more detailed (D) and (E) are more representative. The greater noise in (D) results from lower precision of the Pliocene Mediterranean Δ_{SL} record. (**F**) Schematic illustration of the nature of the relationships in (A) to (E). In (F), 1 represents the trajectory associated with gradual ice-volume buildup, determined by continuous instantaneous ice volume–based adjustment of δ_p, and lagged adjustment of $\overline{\delta_{ice}}$ according to the residence-time calculation discussed in Methods (Eqs. 12 to 14). 2 represents rapid ice loss during deglaciation that occurs at the $\overline{\delta_{ice}}$ value attained just before deglaciation onset; and 3 represents adjustment at the end of deglaciation, when new ice starts to build up at the starting δ_p value. 4 is the trajectory associated with gradual partial glaciation (as 1), 5 is rapid partial deglaciation (as 2), and 6 represents more gradual $\overline{\delta_{ice}}$ adjustment to conditions commensurate with the remaining ice volume after partial deglaciation.

that the Red Sea record may underestimate sea level at that time. All Middle Pliocene sea level benchmarks shown (*49*, *50*) agree with our Δ_{SL}, although the youngest does so only at its extreme age uncertainty. Our Δ_{SL} may offer a means to refine age estimates for benchmarks with relatively large dating uncertainties at times of large Δ_{SL} variations.

Agreement with the 800-ka multiproxy sea level stack (Figs. 2B and 3A) (*12*) cannot be used for validation because it underpins the regression that provides our Δ_{SL} (Methods and fig. S3). In addition, we note that a previous δ_c-based Δ_{SL} deconvolution (*4*) also agrees well with our Δ_{SL} between 0 and 3 Ma ago, albeit at somewhat muted amplitudes with glacials only reaching −100 m (Fig. 3A). Between 3 and 5.3 Ma ago (Fig. 3A), and extending to 13 Ma ago (Fig. 4A), however, that record (*4*) has much less Δ_{SL} variability than our results, which requires comparison with additional independent evidence.

In the 3.3– to 3.0– and 2.9– to 2.65–Ma ago intervals, amplitude variations in both our Δ_{SL} record and the previous δ_c-based record (*4*) agree with maximum relative sea level amplitude ranges of up to 27 and 35 m in New Zealand, respectively (Fig. 3A) (*52*). However, Middle Pliocene sea level benchmarks (Figs. 3A and 4A) (*49*, *50*) and Miocene best and maximum sea level amplitude estimates from New Jersey and the Delaware Coastal Plain (Fig. 4A) (*53*) indicate that the previous δ_c-based Δ_{SL} deconvolution (*4*) is anomalously flat and low between 3 and 13 Ma ago and that its amplitude variations between 13 and 22 Ma ago exceed independently established amplitude constraints (*53*). In contrast, our Δ_{SL} record agrees well with both these independent lines of evidence (Figs. 3A and 4A). The difference may arise from the fact that our method operates in the same way across all time frames, based on generic warm and cold ice sheets. In contrast, that of de Boer *et al.* (*4*) was primarily set up to account for LIS and EIS variations, driven by mid-latitude to subpolar northern hemisphere temperatures inferred from δ_c, and used a tuning factor for AIS so that a large V_{AIS} response was obtained across the EOT. Possibly, the tuning factor used by de Boer *et al.* (*4*) is too strong, resulting in overly sensitive V_{AIS} responses through the Oligocene-Miocene, achieving a "full" AIS state that allowed no further expansions, which results in a flat Δ_{SL} curve until northern hemisphere glaciation began. Alternatively, the assumption that mid-latitude to subpolar northern hemisphere temperatures could be inferred from δ_c (*4*) may be incorrect.

We favor the latter explanation, on the basis of comparison of our calculated T_w variations with independently determined Antarctic temperature variations at European Project for Ice Coring in Antarctica (EPICA) Dome C (EDC) (Fig. 3C) (*54*). This reveals excellent amplitude structure agreement between our T_w and T_{EDC}, scaled as $\Delta T_w \approx 0.25\ \Delta T_{EDC}$. Offsets in this comparison only concern the chronologies between the two records, between 0.4 and 0.7 Ma ago. We infer that global mean deep-ocean temperature has consistently been set by temperature fluctuations in high southern latitudes rather than in the mid-latitude to subpolar northern hemisphere as was assumed previously (*4*). This is an important observation for understanding ocean-atmosphere feedbacks on these time scales. In addition, this observation may help in developing chronologies for old (partially deformed) ice-core sections and blue-ice sections, which are difficult to date because they lack stratigraphic continuity [e.g., (*55*, *56*)], by adding independent age controls from T_w matching.

We also compare our T_w record with a 1.6-Ma Mg/Ca reconstruction for Ocean Drilling Program (ODP) Site 1123 from Chatham Rise, east of New Zealand (3290 m in water depth) (*16*). Reasonable agreement exists over the interval 0 to 1.2 Ma ago (Fig. 3C). Offsets occur at 1.3 to 1.45 Ma ago, where the Mg/Ca record suggests T_w drops to −4°C relative to present. Given a modern in situ bottom-water temperature of just above 1°C at Site 1123 (*15*) and adjustment to potential temperature of less than −0.2°C, a −4°C T_w drop at Site 1123 would suggest deep-water formation at surface temperatures just under −3°C. This is considerably below the seawater freezing temperature of about −1.8°C, which suggests that there is an issue with the

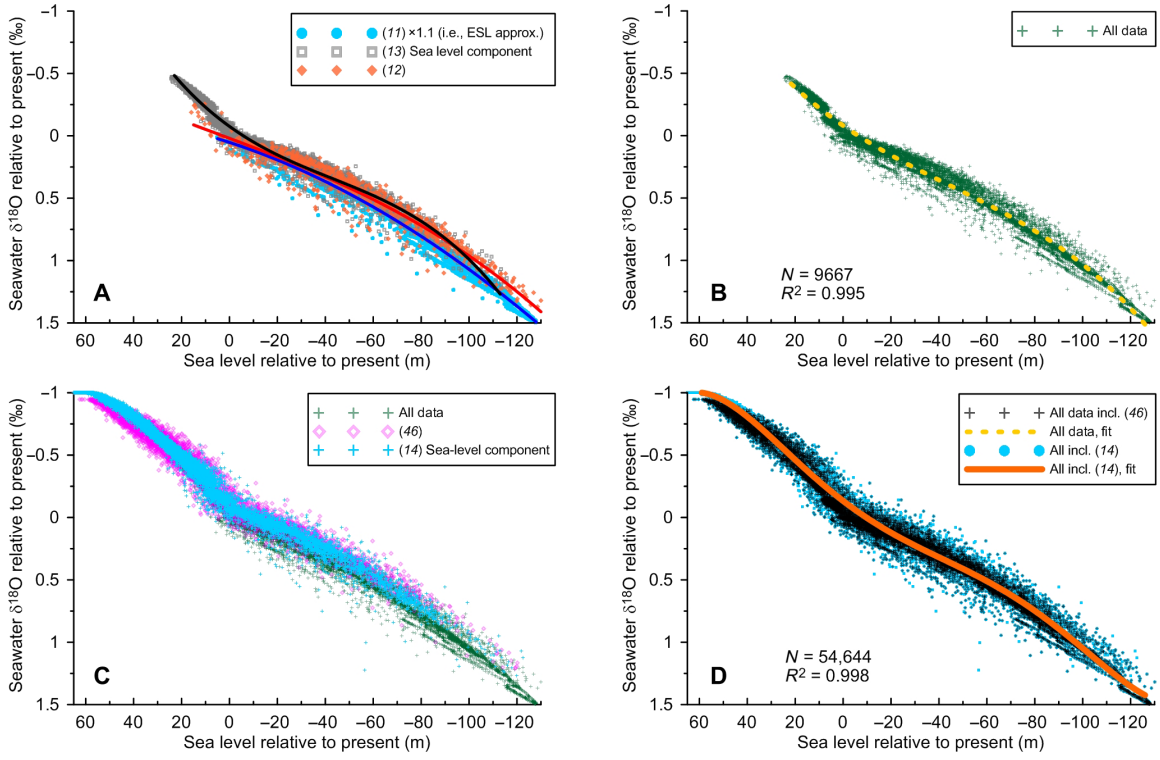

Fig. 6. Regressions between Δ_{SL} and $\Delta\delta_w$. (**A**) Regressions based on runs for three individual sea level approximations: light and dark blue based on the Red Sea record (*8*–*11*); orange and red based on a stack of different records (*12*); and gray and black based on a lag-optimized quadratic regression between benthic δ_c (*13*) and the sea level stack (*12*), forced to peak at Δ_{SL} = 65.1 m (fig. S3). (**B**) All data from (A) combined, with regression in yellow. (**C**) As (B) with superimposed (magenta) results from a run based on the Mediterranean Sea record (*46*) and (light blue) results based on benthic δ_c (*13*) and the sea level stack of different records (*12*), constrained to peak at Δ_{SL} = 65.1 m. (**D**) Black = green + magenta data from (C), and blue is all three datasets from (C) combined with regression in orange. The regression is a fifth-order polynomial for optimal visual fit through the inflection in the data cloud with least edge effects: $\Delta\delta_w = 9.6\times10^{-11}\Delta_{SL}^5 + 1.9\times10^{-8}\Delta_{SL}^4 + 2.5\times10^{-7}\Delta_{SL}^3 - 1\times10^{-4}\Delta_{SL}^2 - 0.015\Delta_{SL} - 0.133$.

Mg/Ca record in this interval. Additional temperature validation is provided by ice-core noble gas analyses, which indicate an LGM global mean ocean cooling of −2.57° ± 0.24°C (*57*), which agrees with our LGM global deep-sea cooling of −2.5° ± 0.3°C (Fig. 3, C and D). However, Mg/Ca temperatures at Site 1123 suggest LGM cooling of only −1° to −1.5°C (Fig. 3D).

The ODP Site 1123 Mg/Ca-based T_w has been used with coregistered δ_c to calculate δ_w (*16*). These data were later used as part of a three-record stack for the interval 0.35 to 1.45 Ma ago (*58*). These δ_w records compare reasonably with our δ_w results, especially in glacial intervals (Fig. 3E). This is a valid comparison to add to the T_w comparison because observational studies primarily resolve T_w and secondarily infer δ_w, while the opposite applies to the present study (fig. S2). Moreover, the studies use independent δ_c records. Additional δ_w validation comes from marine-sediment pore-water δ_w measurements. These reveal an LGM-modern gradient of about 1 ± 0.1‰ (*20*–*22*), while we find 1.1 to 1.4‰ across the different runs; namely, 1.4‰ in the Red Sea–based example (*8*–*11*), 1.4‰ in the example for the statistical multiproxy sea level stack (*12*), 1.2‰ in the Mediterranean-based example (*46*), 1.1‰ based on our δ_c-to-Δ_{SL} conversion using the benthic stack (*13*), and 1.2‰ based on our δ_c-to-Δ_{SL} conversion using the benthic megasplice (*14*). The difference likely falls within assumptions and uncertainties in both methods, especially given that reevaluation of the pore-water method has indicated larger uncertainties (*22*) than considered originally (*20*, *21*).

In Fig. 4B, additional validation criteria labeled *3a*, *3b*, and *5* indicate broad validation of key northern hemisphere (LIS + EIS + GrIS) glaciation stages (red) with ice-rafted debris (IRD) records from the Nordic Seas and wider North Atlantic (*59*, *60*) and previous inferences of an onset of ephemeral or partial northern hemisphere ice development, respectively (*1*). Criterion *4* corroborates V_{AIS} fluctuations (*61*), while *6* marks agreement about the end of the most recent intermittently ice-free period (*3*); we note that *4* and *6* are not fully independent because they partly rely on δ_c information (*3*, *61*). AIS glaciation onset at the EOT (criterion *7*) marks a well-studied greenhouse-icehouse transition that provides binary validation (ice versus no ice) although some suggest somewhat earlier major glaciation from ~36 Ma ago (*47*). In addition, a δ_w change of 0.35 ± 0.12‰ has been inferred across the Middle Miocene Climate Transition (MMCT) (*62*), which agrees well with our results (criterion *8*). Last, a Mg/Ca-based T_w compilation over a broad Eocene-Oligocene interval indicates excellent agreement with our result between 37.5 and 40 Ma ago (criterion *9a*) and reasonable agreement for the lowest T_w values around the EOT (criterion *9b*; allowing for potential chronological offsets). In the Early and Middle Oligocene, values in the Mg/Ca compilation generally fall ~1°C above our estimates, albeit just within uncertainties. Between 31 and 28 Ma ago and after 26 Ma ago, this offset is reduced noticeably so that values agree well within uncertainties.

Use of multiparameter approaches to validate our reconstructions goes a long way to excluding potential diagenetic impacts on

benthic δ_c. Following our method, diagenetic alteration of δ_c to more positive (negative) values would cause spuriously low (high) Δ_{SL} anomalies that would imply larger (smaller) ice volume. This, in turn, would drive positive (negative) $\Delta\delta_w$ anomalies, whose subtraction from more positive (negative) δ_c would have a canceling effect, resulting in reconstruction of minor to negligible T_w changes. The only interval with limited (though still substantial) T_w variability is between 13 and 5 Ma ago (Fig. 4D), but Δ_{SL}, AIS volume, and onset of northern hemisphere ice presence from our method remain well validated (criteria *1*, 2, *4*, and *5*; Fig. 4, A and B), which indicates that low T_w variability in this interval does not arise from diagenetic alteration of δ_c.

There are also some discrepancies. Deep-sea cooling at the MMCT was estimated at 1.5° ± 0.5°C (*62*), which is ~1°C less than inferred here (discrepancy *iv*, Fig. 4D). In addition, at around that time, large-amplitude Δ_{SL} fluctuations have been inferred from stratigraphic analyses of northeastern Australian sequences (Fig. 4A, discrepancy *i*) (*63*). However, these disagree not only with our results but also with the Δ_{SL} record of de Boer (*4*) and with criterion *2* (*53*). Discrepancies *ii* and *iii* are now evaluated in more detail.

Previous cumulative EOT Δ_{SL} estimates reach −70 to −80 m (*3*, *64*), which greatly exceed our estimate of about −30 m (discrepancy *ii*). The Δ_{SL} record of de Boer (*4*) indicates about −45 m of sea level change across the EOT (accounting for different pre-EOT values in Fig. 4A), similar to −30- to −50-m estimates of relative sea level fall from New Jersey Coastal Plain backstripping analysis (*65*); both are closer to our estimate than to the −70- to −80-m estimates. This EOT Δ_{SL} discrepancy must be considered together with the difference between Mg/Ca-based ~2.5°C EOT cooling (*66*) and our inferred ~3.5°C cooling (Fig. 4D, discrepancy *iii*). The ~1°C difference scales to ~0.25‰ in $\delta^{18}O$. Given that the AIS at the time was only beginning to grow, its $\overline{\delta_{ice}}$ would not have been very negative. This is evident in Fig. 4 where $\Delta\delta_w$ = 0.25‰ for Δ_{SL} = −30 m at the EOT. If the ~2.5°C EOT cooling (*66*) is correct—which remains to be settled in view of agreement between our results and both high Eocene and lowest EOT T_w [criteria *9a* and *9b* (*67*)]—then the implied 0.25‰ of "missing" $\delta^{18}O$ would correspond to another −30 m of Δ_{SL}, giving a total of −60 m that is similar to the modern V_{AIS}. Moreover, AIS may, at the time, have behaved more like a warm ice sheet (similar to the Pleistocene LIS and EIS), with early-growth $\overline{\delta_{ice}}$ only around −25‰ and full-size $\overline{\delta_{ice}}$ only around −40‰ (*68*). This would make the Δ_{SL} of −60 m an underestimate and bring potential values closer to previous −70- to −80-m estimates (*64*). If this were the case, then a fundamental shift is implied in the global $\Delta\delta_w$:Δ_{SL} relationship at some stage between 34 and 22 Ma ago. This might be related to a Rayleigh distillation change over the AIS from warm ice sheet behavior to cold ice sheet behavior so that the $\Delta\delta_w$:Δ_{SL} relationship in Fig. 6 would apply only to later times (<22 Ma ago). It is also possible that Mg/Ca-based T_w estimates across the EOT are problematic; for example, because of ocean Mg concentration changes and carbonate saturation changes (*69*). Western Ross Sea sedimentary cycles suggest that sea level oscillations only reached ~20-m amplitudes across the EOT, similar to our Δ_{SL} (*70*). Given literature disagreement about sea level and T_w changes across the EOT, it is not yet possible to either accept or reject our Δ_{SL} result for that event.

Important evidence that is used to argue for large EOT V_{AIS} buildup (or starting 36 Ma ago) concerns an onset of IRD deposition in marine sediments around Antarctica (*47*, *71*), which indicates that ice large enough to support calving had (in places) made it to the coast. On the basis of the size of the continent and the general parabolic cross-sectional profile of ice sheets, this suggests, at first glance, that an ice sheet of roughly modern proportions had built up. However, similar arguments have been rejected for the Early Pleistocene LIS, on the basis of the fact that ice sheets on slippery regolith would remain much lower (because of reduced bed friction) and less voluminous than ice sheets positioned on bedrock after earlier glaciations removed most regolith (*72*–*74*). We propose that consideration must be given to the possibility that the EOT AIS may have been less like the present-day AIS and more like an Early Pleistocene low-slung, slippery LIS (*72*–*75*), which might explain IRD deposition even with V_{AIS} only about half its present-day value. Our results suggest that a consistently large-volume/high AIS existed only since about 13 Ma ago (Figs. 4D and 7A).

Wider implications

In our reconstructions, before deep northern hemisphere glaciations started 3 to 2.5 Ma ago, mean global deep-sea temperatures remained a few degrees above freezing, which indicates substantial deep-water supply from nonfreezing regions (Figs. 3, C and D, 4D, and 7D). Relative to the Late Pleistocene mean, T_w was 2° to 3°C higher at 3 to 13 Ma ago, 3° to 5°C higher at 15 to 33.5 Ma ago, and 7° to 9°C higher at 34.5 to 40 Ma ago, marking distinct quasi-stable states that remain evident when considering variability around those means (pale red, orange, and blue rectangles in Fig. 7D). These ranges and an absence of outlier patterns in our mutually consistent Δ_{SL}, $\Delta_{\delta w}$, and Δ_{Tw} reconstructions (Supplementary Materials) indicate that no major warm, saline deep-water contributions existed throughout the time scales investigated and that high-latitude deep-water formation processes were dominant.

The existence of quasi-stable T_w states is consistent with similar reconstructed ice volume behavior, which suggest virtually no ice before 34 Ma ago, small-to-mid size Antarctic ice at 15 to 33.5 Ma ago, and small-to-full size Antarctic ice with small northern hemisphere ice at 3 to 13 Ma ago (pale red, orange, and blue rectangles in Fig. 7A). These quasi-stable periods are separated by major transitions: the EOT, the end of the Middle Miocene Climatic Optimum (MMCO) and the Plio-Pleistocene transition to extensive bipolar glaciation (yellow bars in Fig. 7D). This resembles critical transition behavior in complex dynamical systems, where variance and autoregression increases occur before transitions (*76*). Variance analysis (Methods and Fig. 7D) reveals that Δ_{Tw} variance increased well before each transition—at ~38.2 Ma ago [previous work suggests ~37 Ma ago (*76*) and longer time series need to be considered to more precisely identify this onset in our method], 17.2 or even 24.8 Ma ago, and 6 Ma ago (dashed purple lines and magenta arrows in Fig. 7D)—and culminated during the transitions. Given that this is consistent with expectations for critical transitions in complex dynamical systems (*76*), we explore the potential drivers behind this behavior.

Earth's climate system has diverse feedbacks that operate over different time scales, including short-term variability/"noise" (*77*, *78*). Insolation, a key external climate forcing, is governed by astronomical cycles that lack multimillion-year trends (*79*) but that can precondition the system for major state changes at certain times (*80*, *81*). Ice-albedo feedbacks operate over time scales that are too short to cause multimillion-year secular changes, but they will amplify any initial change as part of a feedback cascade, aiding transitions in regimes with multiple stable states. Plate tectonics is a suitable candidate for causing multimillion-year secular atmospheric CO_2 changes and

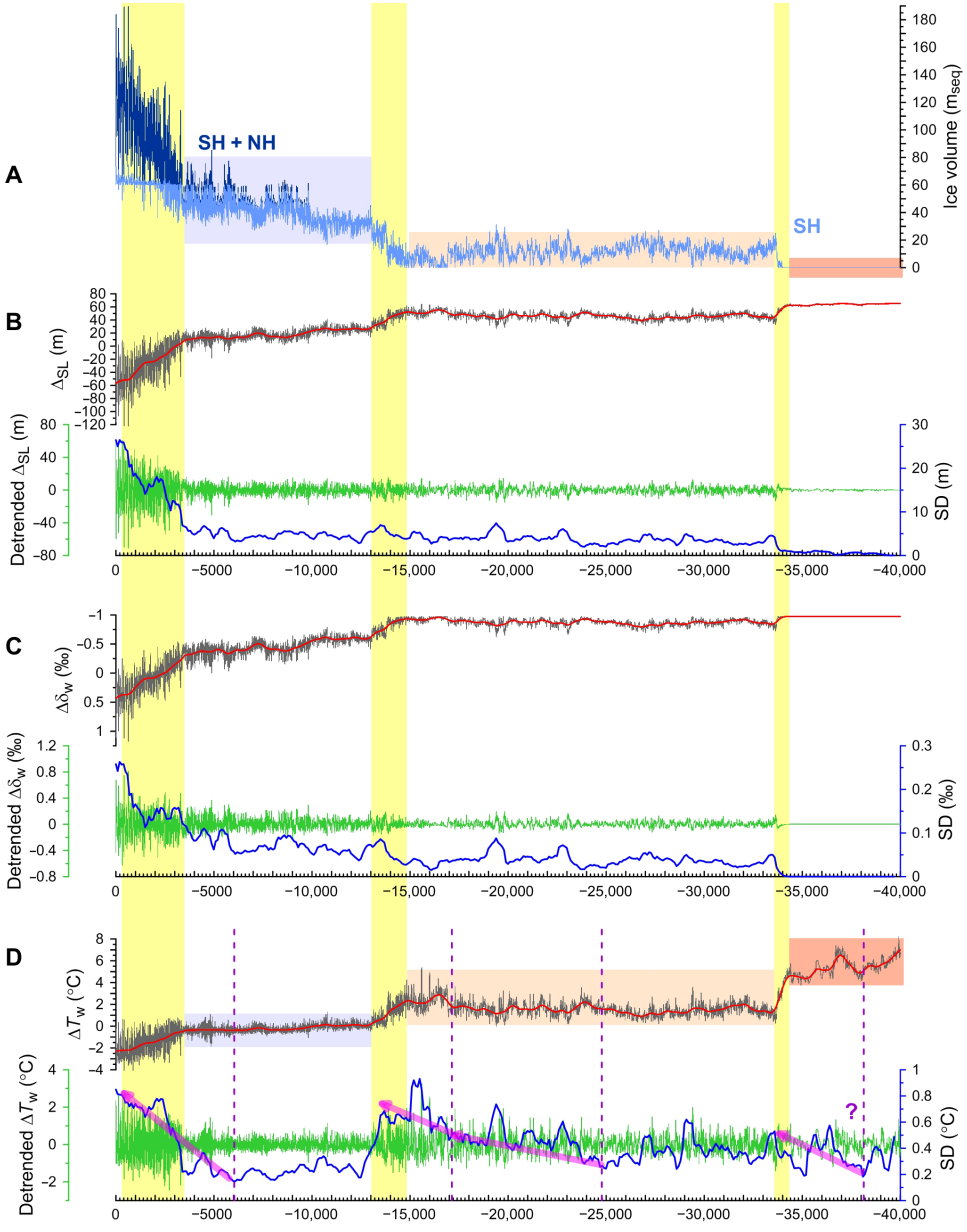

Fig. 7. Variance analyses. (**A**) Reconstructed ice volume in m_{seq} for the southern hemisphere (SH) alone (AIS; light blue) and the global total (AIS plus GrIS, LIS, and EIS; dark blue). NH, northern hemisphere. (**B**) Sea level variations (gray), with trend line (red; see Methods), detrended sea level variations (green), and variance analysis [standard deviation (SD) per moving 500-ka window; blue]. (**C**) As (B) but for deep-seawater $\delta^{18}O$ variations. (**D**) As (B) but for deep-sea temperature variations. Pale red, orange, and blue rectangles outline quasi-stable states, and yellow bars indicate transitions, as discussed in the text. Pale purple arrows indicate phases of T_w variance buildup, starting at around the times indicated with dashed purple lines. The question mark for the variance buildup from ~38.2 Ma ago indicates uncertainty in pinpointing the start of this process in records limited to the past 40 Ma. We used as guidance a study that identified an age of ~37 Ma ago for this event (*76*).

hence climate, through subtle but long-lasting modifications of the balance between volcanic CO_2 outgassing and weathering-related CO_2 sequestration (*82*). Note that this concerns long-term exogenic CO_2 trends related to plate tectonics rather than shorter endogenic CO_2 variations related to carbon-cycle feedbacks. CO_2 levels changed from ~1000 parts per million (ppm) at around 40 Ma ago to ~180 ppm during Late Pleistocene glacial stages and ~280 ppm during interglacials (*83*–*85*), which spans roughly two 2× CO_2 changes. Given that radiative forcing change for each 2× CO_2 change amounts to almost 4 Wm^{-2} (*86*), the CO_2 reduction since 40 Ma ago amounts to roughly 8 Wm^{-2} reduction in radiative climate forcing. This represents 5° to 9°C cooling based on a 5 to 95% range for equilibrium climate sensitivity (*86*), in agreement with the 6°C cooling in our reconstructed T_w (Fig. 7D).

While major climate transitions separating relatively stable states are known from benthic δ_c compilations (*1*–*3*, *14*), we have deconvolved these records into the contributing ice-volume and deep-sea temperature components. Adjusting more rapidly than ice volume,

T_w represents a more direct reflection of global climate variability, while ice volume provides a longer time-integrated view of the changing climate state. We propose that long periods of increasing T_w variance ("flickering") before the detected state transitions (Fig. 7) represent periods when gradually declining CO_2 reached levels where multiple stable climate states exist (*78*, *87*), the existing warmer state that supports less ice and a colder state that supports more ice. Stochastic shocks play an important role in triggering transitions before bifurcation points (*87*). We propose that cold- or warm-biased organization of climate system noise during cold or warm orbital extremes provided these shocks [akin to stochastic or nonlinear resonances; (*78*, *88*)], similar to model-based findings for the EOT (*81*).

We emphasize that the entire past 40 Ma investigated here is dominated by cooling; apart from the MMCO onset, the interval contains no significant long-term warming. Our evidence, therefore, is largely indicative of transitions in the cooling direction, although inferences can also be made about potential warming transitions. Existence of long (2 Ma or more) flickering intervals preceding the detected transitions (Fig. 7) suggests that bistable regimes existed over long time periods. The eventual transition to a colder stable state with greater ice volume, therefore, likely occurred at a considerably lower CO_2 threshold value than the return to a warmer stable state with smaller ice volume because of stabilizing feedbacks associated with large ice masses (*89*). Similar behavior has been inferred from Antarctic ice sheet modeling experiments, where the hysteresis relative to CO_2 levels spans hundreds of parts per million (*90*). Using the bounds of flickering intervals in our reconstructions (Fig. 7), we infer that bistable regimes existed between at least 0 and 6 Ma ago, between 12.6 and 17.2 Ma ago, and—less well defined in our results—between 34 and 38.2 Ma ago. Precise CO_2 reconstructions for those intervals may help to quantify climate state hysteresis relative to CO_2, with implications for understanding potential future climate transitions.

Application and outlook

Our mutually consistent, process-based framework for reconstructing Δ_{SL}, V_{ice}, δ_{ice}, T_w, and δ_w permits complete system validation using multiple parameters rather than only one or two as in traditional approaches. It also helps to identify unrealistic single-parameter fluctuations and/or to fill in information across data gaps so that more complete records can be obtained. Last, our results offer continuous, quantitative context to data from analytical methods such as sea level benchmarking or novel T_w assessment (e.g., clumped isotopes) with low temporal resolution and/or age uncertainties that preclude precise attribution to specific climate cycles.

Our mutually consistent Δ_{SL}, δ_{ice}, T_w, and δ_w records are well validated over at least the past 22 Ma, which comprise the full −130- to +65.1-m range of sea level variation. Validation is not (yet) as convincing for earlier times, so we infer that our Δ_{SL} record (black in Fig. 4A) offers a well-validated sea level record only for the past 22 Ma; this record is obtained using $\Delta_{SL} = -8.4\,\delta_c^2 + 6.8\,\delta_c + 65.1$, where δ_c is normalized to the most recent value of 3.23‰ in the Lisiecki and Raymo benthic δ_c stack (*13*). The two regression extremes (pink and orange in Fig. 4A) provide realistic total range bounds (for equations, see fig. S3). Before 22 Ma ago, our Δ_{SL} results require further validation. Note that our assessment concerns orbital and longer time scale sea level variability and that no conclusions should be drawn with respect to millennial sea level variability without further extensive testing.

We find close amplitude structure agreement between our calculated T_w variations and independently determined Antarctic temperature variations at EDC (*54*), scaled as $\Delta T_w \approx 0.25\,\Delta T_{EDC}$ (Fig. 3C). This stunning independent agreement provides strong validation of our approach. We infer that global mean deep-ocean temperature has consistently been set by high southern-latitude temperature fluctuations.

Diverse positive validations also indicate that our inferred $\Delta\delta_w$:Δ_{SL} relationships offer reasonable approximations of reality. Hence, we propose that ice-volume/sea level reconstruction based on δ_w records from T_w-corrected δ_c data, or ice-volume corrections of δ_w records to identify regional hydrological influences, should no longer use linear transformations. Instead, we propose that improved results will be obtained using the nonlinear relationship found here through all instances (N = 54,644). The optimum regression fit to capture the shape of the data cloud is $\Delta\delta_w = 9.6 \times 10^{-11}\Delta_{SL}^5 + 1.9 \times 10^{-8}\Delta_{SL}^4 + 2.5 \times 10^{-7}\Delta_{SL}^3 - 1 \times 10^{-4}\Delta_{SL}^2 - 0.015\Delta_{SL} - 0.133$. While polynomial orders higher than cubic do not statistically significantly improve the relationship, the fifth-order fit visually best captures the nonlinearity that is theoretically evident, with the least edge effects, and offers the best conversion equation.

Further research is needed to hone the approach presented here. A particularly promising route is to develop V_{ice}:δ_p transforms using geographically specific, less idealized, δ^{18}O-enabled ice sheet models that account for additional controls on δ_p (*26*), which can then be applied to the various ice sheet growth histories to determine more realistic $\overline{\delta_{ice}}$ histories for each ice sheet. We advocate use of these transforms because integrating fully coupled δ^{18}O-enabled ice sheet models over many millions of years will be computationally challenging. Making the suggested transform functions will provide a sound middle way between that and our use of idealized scenarios. In addition, there is a need for further paleoclimate and paleoceanographic benchmarks; for example, to resolve the origins of changes around the EOT and to provide further Oligocene-Miocene data for improved validation. Last, more detailed understanding of Mg/Ca changes over the past 40 Ma would improve deep-sea temperature reconstructions and facilitate more advanced validation of the approach presented here.

Our data-driven reconstructions suggest that climate-system changes during the descent from Eocene greenhouse to Late Pleistocene icehouse conditions were not gradual but comprised sharp threshold-like adjustments (critical transitions) between quasi-stable states. By analogy, it seems important for future climate change projections to allow for historically unprecedented adjustments, such as deep-water formation shifts, abrupt (partial) ice sheet collapse, or other cascading feedbacks.

METHODS

Δ_{SL} from δ_c records

Calculation of sea level change (Δ_{SL}) from benthic δ_c records (*13*, *14*) was undertaken using second-order polynomial regressions based on the lag-optimized comparison between δ_c and a statistical sea level assessment based on a variety of input data (*12*). The regressions and their equations are given in fig. S3. Uncertainty bounds account for both the regression uncertainty and additional data uncertainties in both X and Y directions. For the latter, we used normal distributions with 1σ = 0.1‰ for δ_c and 1σ = 2 m for Δ_{SL}.

Isotope fractionation over the ice sheets

δ_p is determined in the main case of the analytical assessment using Eq. 1 and for sensitivity test 1 using Eq. 2. Constants were selected to achieve a reasonable visual fit through modern ice sheet values (fig. S1). For the main case of our analytical assessment and the subsequent applied assessments, we use a heuristically fitted function representative of the described trends that start with an initial snow $\delta_p = -15‰$ that drops rapidly with initial ice sheet volume buildup, followed by an exponential change with V toward very negative values over large-scale ice sheets (fig. S1). To this end, we use an equation of the form

$$\delta_p = \alpha e^{\left\{\frac{(0.9V-10)}{63}\right\}^2}(100 - V) - (C + 15) \quad (1)$$

Here, C is a constant that is adjusted along with amplitude parameter α so that initial precipitation (for ice sheet volume $V = 0$ m_{seq}) is precisely −15‰ in all cases. Extreme Rayleigh distillation at the isolated, high-latitude AIS causes very negative δ_p (*42*), which, in Eq. 1, requires $\alpha = 1$ (with $C = 102.55$). GrIS is set to the same parameters. In contrast, a lower α is needed for LIS (and EIS) to account for less negative δ_p in response to more limited Rayleigh distillation between evaporative sources and precipitation sites, related to their positions in lower latitudes closer to relatively warm oceanic moisture sources. An $\alpha = 0.55$ value (with $C = 56.4$) is used for LIS to reach a minimum LGM δ_p of roughly −35‰, as suggested by five isotope-enabled global climate circulation models (*35*). EIS is set to the same parameters.

Sensitivity test 1 instead uses linear δ_p changes (Eq. 2), although this is physically implausible. For AIS and GrIS, the slope-defining constants J and K are set to −60 and 66.3, respectively, and for LIS and EIS, these are set to −25 and 26, respectively, to get reasonable agreement with δ_p observations (fig. S1)

$$\delta_p = V\frac{J - 15}{K} - 15 \quad (2)$$

In sensitivity test 2, AIS glaciation is set to an arbitrary quadratic function so that AIS grows less rapidly during initial glaciation stages and more rapidly during later stages. The sea level budget is closed by setting an opposite LIS-volume anomaly. This is explored to evaluate impacts on the solution, which are found to be negligible.

Ice sheet and seawater $\delta^{18}O$

The global volume-weighted (here equivalent to mass-weighted) mean oxygen isotope composition of ice is given by

$$\delta^*_{ice} = \frac{\delta_{ice\_AIS}V_{AIS} + \delta_{ice\_GrIS}V_{GrIS} + \delta_{ice\_LIS}V_{LIS} + \delta_{ice\_EIS}V_{EIS}}{V_{tot}} \quad (3)$$

The imposed global seawater $\delta^{18}O$ change is found using

$$\Delta\delta_w = -\frac{0.9\,V_{tot}\,\delta^*_{ice}}{V_{oc} + \Delta_{SL}} \quad (4)$$

Here, 0.9 is the ice-to-water density ratio, V_{oc} is global ocean volume (3700 m_{seq}), and $\Delta_{SL} = -\{(V_{AIS} - 57.8) + (V_{GrIS} - 7.3) + V_{LIS} + V_{EIS}\}$. Note that, throughout, we consider ice-volume change to be inversely proportional to sea level change, accounting for density differences between water and ice. This is a simplification because some ice sheet portions may displace water so that they do not contribute to sea level change, whereas they do count toward ice-volume (and thus δ_w) change [e.g., (*37*)].

Individual ice sheet volume histories

In our applied assessments, Δ_{SL} (in meters relative to present) is used to determine global net ice loss or gain per time step j (forward in time). Ice sheets are grown in relation to Δ_{SL} using prescribed conditional functions. Note that we do not fully reduce the functions below, so it will be clearer what is calculated. AIS volume per time step is given by

$$V_{AISj} = \begin{cases} 57.8 + \frac{-\Delta_{SLj}}{2} \text{ if } 0 < 7.3 + \frac{-\Delta_{SLj}}{2} \le 7.3 \\ 57.8 - \Delta_{SLj} \text{ if } 7.3 < \Delta_{SLj} \le 57.8 \\ 0 \text{ if } 57.8 < \Delta_{SLj} \\ V_{AISj-1} + \frac{-z_{min}}{125}15\left(\frac{-\Delta_{SLj}}{z_{min}}\right)^2 \text{ otherwise} \end{cases} \quad (5)$$

Here, 57.8 stands for modern V_{AIS} (in m_{seq}), 7.3 for modern V_{GrIS} (in m_{seq}), 15 for the assumed LGM V_{AIS} addition (in m_{seq}), Δ_{SL} for sea level position per time step (in meters relative to present), z_{min} for the maximum sea level drop in the Δ_{SL} record used, and V_{AISj-1} at run initialization is simply set at modern V_{AIS} (hence, all runs have an initialization period during which the solution stabilizes). The squared term in the last row provides a nonlinear AIS-excess buildup during further glaciation, relative to present, to approximate observations of less excess-ice growth at earlier stages and greater growth at later glacial stages (*38*).

GrIS volume is calculated similarly (with assumed LGM V_{GrIS} addition of 5 m_{seq}), as

$$V_{GrISj} = \begin{cases} 7.3 + \frac{-\Delta_{SLj}}{2} \text{ if } 0 < 7.3 + \frac{-\Delta_{SLj}}{2} \le 7.3 \\ 0 \text{ if } 7.3 + \frac{-\Delta_{SLj}}{2} \le 0 \\ V_{GrISj-1} + \left(\frac{-z_{min}}{125}5\frac{-\Delta_{SLj}}{z_{min}}\right) \text{ otherwise} \end{cases} \quad (6)$$

For LIS and EIS combined, which exist only when $\Delta_{SL} < 0$ m, linear growth is determined in proportion to the Δ_{SL} record. However, between them, we assume that one dominates growth in initial glaciation stages, with the other catching up at later stages, to roughly mimic moisture scavenging effects between ice sheets due to large-scale atmospheric circulation changes (*91*). This is done in a similar fashion to sensitivity test 2 of the analytical assessment with an arbitrary nonlinear gradient function, calculated for each time step

$$G_j = 1 - (0.5e)^{20\frac{\Delta_{SLj}}{-z_{min}}} \quad (7)$$

EIS volume is simply calculated taking into account this gradient function, and V_{LIS} in addition compensates for the nonlinearity stipulated in V_{AIS} at $\Delta_{SL} < 0$ m, to ensure that total ice-volume changes remain balanced with Δ_{SL} (within rounding errors).

To calculate V_{LIS}, there is a first step

$$V_{xj} = \begin{cases} \left(\frac{-z_{min}}{125}70\frac{-\Delta_{SLj}}{-z_{min}}\right)G_j - \left(\frac{-z_{min}}{125}15\frac{\Delta_{SLj}}{z_{min}} + \frac{-z_{min}}{125}15\left(\frac{-\Delta_{SLj}}{z_{min}}\right)^2\right) \text{ if } -\Delta_{SLj} > 0 \\ 0 \text{ otherwise} \end{cases} \quad (8)$$

Here, 125 m_{seq} stands for the total ice-volume increase corresponding to the assumed LGM Δ_{SL}, 70 m_{seq} for the LIS component (35 m_{seq} for EIS), and 15 m_{seq} for the LGM expansion of V_{AIS}, as before. Then, V_{LIS} is given by

$$V_{LISj} = \begin{cases} V_{xj} \text{ if } 0 \le V_{xj} \le \frac{-z_{min}}{125}\,70 \\ 0 \text{ if } V_{xj} < 0 \\ \frac{-z_{min}}{125}\,70 \text{ otherwise} \end{cases} \quad (9)$$

To calculate V_{EIS}, the first step is

$$V_{sj} = \begin{cases} -\Delta_{SLj}\frac{\frac{-z_{min}}{125}(70+35)}{-z_{min}} - \left(\frac{-z_{min}}{125}\,70\,\frac{-\Delta_{SLj}}{-z_{min}}\right) G_j \text{ if } -\Delta_{SLj} > 0 \\ -\Delta_{SLj}\frac{\frac{-z_{min}}{125}(70+35)}{-z_{min}} \text{ otherwise} \end{cases} \quad (10)$$

In addition, V_{EIS} is then given by

$$V_{EISj} = \begin{cases} V_{sj} \text{ if } 0 \le V_{sj} \le \frac{-z_{min}}{125}35 \\ 0 \text{ if } V_{sj} < 0 \\ \frac{-z_{min}}{125}\,35 \text{ otherwise} \end{cases} \quad (11)$$

Ice sheet weighted mean $\delta^{18}O$ and seawater $\delta^{18}O$

For each ice sheet, the isotopic value of new precipitation (δ_p) is determined per time step using Eq. 1, for AIS and GrIS using $\alpha = 1$ ($C = 102.55$), and for LIS and EIS using $\alpha = 55$ (with $C = 56.4$). To calculate the volume-weighted mean δ_{ice} (i.e., $\overline{\delta_{ice}}$) for each ice sheet, we use a residence-time calculation. This starts with ice sheet gross accumulation rate (a_{grs}) determination based on the area defined by its volume (with constant aspect ratio ε), simply scaled in proportion to a modern global annual a_{grs} of ~0.008 m_{seq} (*44*, *45*) for a global ice volume of 65.1 m_{seq}. Volume is obtained in relation to Δ_{SL} according to Eqs. 5 to 11; volume is true volume (in m^3) rather than scale volume (in m_{seq}); this is indicated using $\boldsymbol{V}$. The term $\Delta_{SL(LIS)}$ is used to indicate the sea level change component attributed to the different ice sheets (here LIS). For a world ocean area A_{oc} of about 362×10^{12} m^2, this gives

$$\boldsymbol{V}_{LISj} = \frac{V_{LISj}A_{oc}}{0.9} \quad (12)$$

For the vertical area under a parabolic profile (with maximum height h_{max}, which is ε times radius r), the mean height is $(^2/_3)h_{max}$ or $(^2/_3)\varepsilon\, r$ so that the volume of our standard planoconvex lens–shaped ice sheet with parabolic cross section is $\boldsymbol{V} = (^2/_3)\varepsilon\,\pi\, r^3$. Solving for r gives the information required to approximate the ice sheet area over which accumulation occurs (here, the example is given for LIS, but it is the same for all others)

$$A_{LISj} = \pi\left(\sqrt[3]{\frac{3}{2}\frac{V_{LISj}A_{oc}}{0.9\varepsilon\pi}}\right)^2 \quad (13)$$

Note that this concerns simply the surface area of the circle occupied by the ice sheet, ignoring the relevant (half) arc length of the parabola because the aspect ratio is so small that both numbers are virtually identical; hence, the circle area was chosen for computational efficiency. The rate a_{grs} over that ice sheet at time step j then is $a_{grsj} = 0.008A_{LISj}/A_{tot(\,mod\,)}$, for a modern global annual a_{grs} = ~0.008 m_{seq} when global ice volume is 65.1 m_{seq}. Here, $A_{tot(mod)}$ is the surface area given by Eq. 13 for the modern total global ice volume of 65.1 m_{seq} (10.7×10^{12} m^2). The model calculates the isotopic contribution from that gross accumulation by its product with δ_p based on Eq. 1. At every time step, gross accumulation is balanced by a gross loss term, which is simply set to a_{grs} minus the sea level change contribution from one time step to the next of the ice sheet considered (here, $a_{netj} = \Delta_{SL(LIS)j} - \Delta_{SL(LIS)j-1}$). The model determines the isotopic impact of a_{netj} using $\overline{\delta_{ice}}_{j-1}$. The calculation is conditional in that periods with negative a_{net} do not lead to changes in $\overline{\delta_{ice}}$

$$\overline{\delta_{ice}}_j = \begin{cases} \overline{\delta_{ice}}_{j-1} \text{ if } a_{netj} < 0 \\ \dfrac{a_{grs_j}\delta_{pj} - (a_{grs_j} - a_{netj})\,\overline{\delta_{ice}}_{j-1} + V_{LISj-1}\,\overline{\delta_{ice}}_{j-1}}{V_{LISj-1} + a_{netj}} \text{ otherwise} \end{cases} \quad (14)$$

Last, a constraint is used that when $\overline{\delta_{ice}}$ from Eq. 14 drops below the model start value $\delta_p = -15‰$ for ice growth, and then $\overline{\delta_{ice}}$ is kept at −15‰. This is done to avoid spurious effects of rounding errors at extremely small ice volumes. We now have, per time step, ice volumes for each ice sheet and their weighted mean ice sheet $\overline{\delta_{ice}}$. Thus, we solve Eq. 4 per ice sheet, per time step, to calculate each ice sheet contribution to a change in mean ocean δ_w using the world ocean volume $V_{oc} = 3700$ m_{seq}, giving (here for LIS)

$$\Delta\delta_{w(LIS)j} = -\frac{0.9\,V_{LISj}\,\overline{\delta_{ice}}_{(LIS)j}}{V_{oc} + \Delta_{SL(LIS)j}} \quad (15)$$

Executed for each ice sheet, their cumulative effects can be determined per time step. The cumulative $\Delta\delta_w$, normalized to the present-day value, can be subtracted from δ_c changes, giving a δ_c residual that indicates bottom-water temperature (T_w) changes based on a change of −0.25‰ per degree Celsius warming.

Thus, we have complete mutual consistency between all key parameters: Δ_{SL}, ice sheet volumes, ice sheet weighted mean $\overline{\delta_{ice}}$, global $\Delta\delta_w$, and T_w. Mutual consistency means that if one changes, so must others. Hence, validation of model results can be undertaken using multiple parameters.

Variance analysis

For the variance analysis, we first detrended the records obtained using the benthic δ_c megasplice (*14*) with a 500-ka moving Gaussian smoothing window. We then calculated SDs of detrended records of residuals over 500-ka windows that were shifted in 100-ka steps across the record. For robustness, we consider only major signals revealed by this analysis. Autoregression analysis (*76*) is precluded because of the (partially) interpolated and/or smoothed nature of the time series considered.

SUPPLEMENTARY MATERIALS

Supplementary material for this article is available at http://advances.sciencemag.org/cgi/content/full/7/26/eabf5326/DC1

REFERENCES AND NOTES

1. J. Zachos, M. Pagani, L. Sloan, E. Thomas, K. Billups, Trends, rhythms, and aberrations in global climate 65 Ma to present. *Science* **292**, 686–693 (2001).
2. J. C. Zachos, G. R. Dickens, R. E. Zeebe, An early Cenozoic perspective on greenhouse warming and carbon-cycle dynamics. *Nature* **451**, 279–283 (2008).

3. K. G. Miller, J. V. Browning, W. J. Schmelz, R. E. Kopp, G. S. Mountain, J. D. Wright, Cenozoic sea-level and cryospheric evolution from deep-sea geochemical and continental margin records. *Sci. Adv.* **6**, eaaz1346 (2020).
4. B. De Boer, R. S. W. van de Wal, R. Bintanja, L. J. Lourens, E. Tuenter, Cenozoic global ice-volume and temperature simulations with 1-D ice-sheet models forced by benthic $\delta^{18}O$ records. *Ann. Glaciol.* **51**, 23–33 (2010).
5. G. L. Foster, E. J. Rohling, Relationship between sea level and climate forcing by CO_2 on geological timescales. *Proc. Natl. Acad. Sci. U.S.A.* **110**, 1209–1214 (2013).
6. M. A. Martínez-Botí, G. L. Foster, T. B. Chalk, E. J. Rohling, P. F. Sexton, D. J. Lunt, R. D. Pancost, M. P. S. Badger, D. N. Schmidt, Plio-Pleistocene climate sensitivity evaluated using high-resolution CO_2 records. *Nature* **518**, 49–54 (2015).
7. E. de la Vega, T. B. Chalk, P. A. Wilson, R. P. Bysani, G. L. Foster, Atmospheric CO_2 during the Mid-Piacenzian Warm Period and the M2 glaciation. *Sci. Rep.* **10**, 11002 (2020).
8. M. Siddall, E. J. Rohling, A. Almogi-Labin, C. Hemleben, D. Meischner, I. Schmelzer, D. A. Smeed, Sea-level fluctuations during the last glacial cycle. *Nature* **423**, 853–858 (2003).
9. E. J. Rohling, K. Grant, M. Bolshaw, A. P. Roberts, M. Siddall, C. Hemleben, M. Kucera, Antarctic temperature and global sea level closely coupled over the past five glacial cycles. *Nat. Geosci.* **2**, 500–504 (2009).
10. K. M. Grant, E. J. Rohling, M. Bar-Matthews, A. Ayalon, M. Medina-Elizalde, C. Bronk Ramsey, C. Satow, A. P. Roberts, Rapid coupling between ice volume and polar temperature over the past 150,000 years. *Nature* **491**, 744–747 (2012).
11. K. M. Grant, E. J. Rohling, C. Bronk Ramsey, H. Cheng, R. L. Edwards, F. Florindo, D. Heslop, F. Marra, A. P. Roberts, M. E. Tamisiea, F. Williams, Sea-level variability over five glacial cycles. *Nat. Commun.* **5**, 5076 (2014).
12. R. M. Spratt, L. E. Lisiecki, A Late Pleistocene sea level stack. *Clim. Past* **12**, 1079–1092 (2016).
13. L. E. Lisiecki, M. E. Raymo, A Pliocene-Pleistocene stack of 57 globally distributed benthic $\delta^{18}O$ records. *Paleoceanogr. Paleoclimatol.* **20**, PA1003 (2005).
14. T. Westerhold, N. Marwan, A. J. Drury, D. Liebrand, C. Agnini, E. Anagnostou, J. S. K. Barnet, S. M. Bohaty, D. De Vleeschouwer, F. Florindo, T. Frederichs, D. A. Hodell, A. E. Holbourn, D. Kroon, V. Lauretano, K. Littler, L. J. Lourens, M. Lyle, H. Pälike, U. Röhl, J. Tian, R. H. Wilkens, P. A. Wilson, J. C. Zachos, An astronomically dated record of Earth's climate and its predictability over the last 66 million years. *Science* **369**, 1383–1387 (2020).
15. H. Elderfield, M. Greaves, S. Barker, I. R. Hall, A. Tripati, P. Ferretti, S. Crowhurst, L. Booth, C. Daunt, A record of bottom water temperature and seawater $\delta^{18}O$ for the Southern Ocean over the past 440 kyr based on Mg/Ca of benthic foraminiferal *Uvigerina* spp. *Quat. Sci. Rev.* **29**, 160–169 (2010).
16. H. Elderfield, P. Ferretti, M. Greaves, S. Crowhurst, I. N. McCave, D. Hodell, A. M. Piotrowski, Evolution of ocean temperature and ice volume through the Mid-Pleistocene Climate Transition. *Science* **337**, 704–709 (2012).
17. D. Evans, W. Müller, Deep time foraminifera Mg/Ca paleothermometry: Nonlinear correction for secular change in seawater Mg/Ca. *Paleoceanogr. Paleoclimatol.* **27**, PA4205 (2012).
18. M. Lebrato, D. Garbe-Schönberg, M. N. Müller, S. Blanco-Ameijeiras, R. A. Feely, L. Lorenzoni, J.-C. Molinero, K. Bremer, D. O. B. Jones, D. Iglesias-Rodriguez, D. Greeley, M. D. Lamare, A. Paulmier, M. Graco, J. Cartes, J. Barcelos e Ramos, A. de Lara, R. Sanchez-Leal, P. Jimenez, F. E. Paparazzo, S. E. Hartman, U. Westernströer, M. Küter, R. Benavides, A. F. da Silva, S. Bell, C. Payne, S. Olafsdottir, K. Robinson, L. M. Jantunen, A. Korablev, R. J. Webster, E. M. Jones, O. Gilg, P. Bailly du Bois, J. Beldowski, C. Ashjian, N. D. Yahia, B. Twining, X.-G. Chen, L.-C. Tseng, J.-S. Hwang, H.-U. Dahms, A. Oschlies, Global variability in seawater Mg:Ca and Sr:Ca ratios in the modern ocean. *Proc. Natl. Acad. Sci. U.S.A.* **117**, 22281–22292 (2020).
19. D. Evans, N. Sagoo, W. Renema, L. J. Cotton, W. Müller, J. A. Todd, P. Kumar Saraswati, P. Stassen, M. Ziegler, P. N. Pearson, P. J. Valdes, H. P. Affek, Eocene greenhouse climate revealed by coupled clumped isotope-Mg/Ca thermometry. *Proc. Natl. Acad. Sci. U.S.A.* **115**, 1174–1179 (2018).
20. D. P. Schrag, G. Hampt, D. W. Murray, Pore fluid constraints on the temperature and oxygen isotopic composition of the glacial ocean. *Science* **272**, 1930–1932 (1996).
21. J. F. Adkins, K. McIntyre, D. P. Schrag, The salinity, temperature, and $\delta^{18}O$ of the glacial deep ocean. *Science* **298**, 1769–1773 (2002).
22. M. D. Miller, M. Simons, J. F. Adkins, S. E. Minson, The information content of pore fluid $\delta^{18}O$ and $[Cl^-]$. *J. Phys. Oceanogr.* **45**, 2070–2094 (2015).
23. W. Dansgaard, Stable isotopes in precipitation. *Tellus* **16**, 436–468 (1964).
24. S. Joussaume, J. Jouzel, Paleoclimatic tracers: An investigation using an atmospheric general circulation model under ice age conditions: 2. Water isotopes. *J. Geophys. Res.* **98**, 2807–2830 (1993).
25. E. J. Rohling, S. Cooke, Stable oxygen and carbon isotope ratios in foraminiferal carbonate, in *Modern Foraminifera*, B. K. Sen Gupta, Ed. (Kluwer Academic, 1999), pp. 239–258.
26. H. C. Steen-Larsen, V. Masson-Delmotte, M. Hirabayashi, R. Winkler, K. Satow, F. Prié, N. Bayou, E. Brun, K. M. Cuffey, D. Dahl-Jensen, M. Dumont, M. Guillevic, S. Kipfstuhl, A. Landais, T. Popp, C. Risi, K. Steffen, B. Stenni, A. E. Sveinbjörnsdottír, What controls the isotopic composition of Greenland surface snow? *Clim. Past* **10**, 377–392 (2014).
27. N. Callow, H. McGowan, L. Warren, J. Speirs, Drivers of precipitation stable oxygen isotope variability in an alpine setting, Snowy Mountains, Australia. *J. Geophys. Res. Atmos.* **119**, 3016–3031 (2014).
28. M. S. Lachniet, D. E. Lawson, H. Stephen, A. R. Sloat, W. P. Patterson, Isoscapes of $\delta^{18}O$ and $\delta^{2}H$ reveal climatic forcings on Alaska and Yukon precipitation. *Water Resour. Res.* **52**, 6575–6586 (2016).
29. C. Tian, L. Wang, K. F. Kaseke, B. W. Bird, Stable isotope compositions ($\delta^{2}H$, $\delta^{18}O$ and $\delta^{17}O$) of rainfall and snowfall in the central United States. *Sci. Rep.* **8**, 6712 (2018).
30. W. Ambach, W. Dansgaard, H. Eisner, J. Møller, The altitude effect on the isotopic composition of precipitation and glacier ice in the Alps. *Tellus* **20**, 595–600 (1968).
31. D. Qin, P. A. Mayewski, C. P. Wake, S. C. Kang, J. Ren, S. Hou, T. Yao, Q. Yang, Z. Jin, D. Mi, Evidence for recent climate change from ice cores in the central Himalaya. *Ann. Glaciol.* **31**, 153–158 (2000).
32. H. Purdie, N. Bertler, A. Mackintosh, J. Baker, R. Rhodes, Isotopic and elemental changes in winter snow accumulation on glaciers in the Southern Alps of New Zealand. *J. Climate* **23**, 4737–4749 (2010).
33. J. V. Hurley, M. Vuille, D. R. Hardy, S. J. Burns, L. G. Thompson, Cold air incursions, $\delta^{18}O$ variability, and monsoon dynamics associated with snow days at Quelccaya Ice Cap, Peru. *J. Geophys. Res. Atmos.* **120**, 7467–7487 (2015).
34. A. Landais, A. Ekaykin, E. Barkan, R. Winkler, B. Luz, Seasonal variations of ^{17}O-excess and d-excess in snow precipitation at Vostok station, East Antarctica. *J. Glaciol.* **58**, 725–733 (2012).
35. G. Ferguson, S. Jasechko, The isotopic composition of the Laurentide Ice Sheet and fossil groundwater. *Geophys. Res. Lett.* **42**, 4856–4861 (2015).
36. M. J. Winnick, J. K. Caves, Oxygen isotope mass-balance constraints on Pliocene sea level and East Antarctic Ice Sheet stability. *Geology* **43**, 879–882 (2015).
37. E. J. Rohling, F. D. Hibbert, F. H. Williams, K. M. Grant, G. Marino, G. L. Foster, R. Hennekam, G. J. de Lange, A. P. Roberts, J. Yu, J. M. Webster, Y. Yokoyama, Differences between the last two glacial maxima and implications for ice-sheet, $\delta^{18}O$, and sea-level reconstructions. *Quat. Sci. Rev.* **176**, 1–28 (2017).
38. Y. Yokoyama, T. M. Esat, W. G. Thompson, A. L. Thomas, J. M. Webster, Y. Miyairi, C. Sawada, T. Aze, H. Matsuzaki, J. Okuno, S. Fallon, J.-C. Braga, M. Humblet, Y. Iryu, D. C. Potts, K. Fujita, A. Suzuki, H. Kan, Rapid glaciation and a two-step sea level plunge into the Last Glacial Maximum. *Nature* **559**, 603–607 (2018).
39. K. Kusahara, T. Sato, A. Oka, T. Obase, R. Greve, A. Aber-Ouchi, H. Hasumi, Modelling the Antarctic marine cryosphere at the Last Glacial Maximum. *Ann. Glaciol.* **56**, 425–435 (2015).
40. R. Staroszczyk, L. W. Morland, Plane ice-sheet flow with evolving orthotopic fabric. *Ann. Glaciol.* **30**, 93–101 (2000).
41. North Greenland Ice Core Project members, High-resolution record of Northern Hemisphere climate extending into the last interglacial period. *Nature* **431**, 147–151 (2004).
42. EPICA community members, Eight glacial cycles from an Antarctic ice core. *Nature* **429**, 623–628 (2004).
43. F. Parrenin, J.-M. Barnola, J. Beer, T. Blunier, E. Castellano, J. Chappellaz, G. Dreyfus, H. Fischer, S. Fujita, J. Jouzel, K. Kawamura, B. Lemieux-Dudon, L. Loulergue, V. Masson-Delmotte, B. Narcisi, J.-R. Petit, G. Raisbeck, D. Raynaud, U. Ruth, J. Schwander, M. Severi, R. Spahni, J. P. Steffensen, A. Svensson, R. Udisti, C. Waelbroeck, E. W. Wolff, The EDC3 chronology for the EPICA Dome C ice core. *Clim. Past* **3**, 485–497 (2007).
44. M. B. Giovinetto, The drainage systems of Antarctica: Accumulation, in *Antarctic Snow and Ice Studies*, M. Mellor, Ed. (American Geophysical Union, 2013), pp. 127–155.
45. R. C. Bales, Q. Guo, D. Shen, J. R. McConnell, G. Du, J. F. Burkhart, V. B. Spikes, E. Hanna, J. Cappelen, Annual accumulation for Greenland updated using ice core data developed during 2000–2006 and analysis of daily coastal meteorological data. *J. Geophys. Res.* **114**, D06116 (2009).
46. E. J. Rohling, G. L. Foster, K. M. Grant, G. Marino, A. P. Roberts, M. E. Tamisiea, F. Williams, Sea-level and deep-sea-temperature variability over the past 5.3 million years. *Nature* **508**, 477–482 (2014).
47. A. Carter, T. R. Riley, C.-D. Hillenbrand, M. Rittner, Widespread Antarctic glaciation during the Late Eocene. *Earth Planet. Sci. Lett.* **458**, 49–57 (2017).

48. A. Dutton, A. E. Carlson, A. J. Long, G. A. Milne, P. U. Clark, R. DeConto, B. P. Horton, S. Rahmstorf, M. E. Raymo, Sea-level rise due to polar ice-sheet mass loss during past warm periods. *Science* **349**, aaa4019 (2015).
49. O. A. Dumitru, J. Austermann, V. J. Polyak, J. J. Fornós, Y. Asmerom, J. Ginés, A. Ginés, B. P. Onac, Constraints on global mean sea level during Pliocene warmth. *Nature* **574**, 233–236 (2019).
50. O. A. Dumitru, J. Austermann, V. J. Polyak, J. J. Fornos, Y. Asmerom, J. Ginés, B. P. Onac, Sea-level stands from the Western Mediterranean over the past 6.5 million years. *Sci. Rep.* **11**, 261 (2021).
51. E. J. Rohling, F. D. Hibbert, K. M. Grant, E. V. Galaasen, N. Irvali, H. F. Kleiven, G. Marino, U. Ninnemann, A. P. Roberts, Y. Rosenthal, H. Schulz, F. H. Williams, J. Yu, Asynchronous Antarctic and Greenland ice-volume contributions to the last interglacial sea-level highstand. *Nat. Commun.* **10**, 5040 (2019).
52. G. R. Grant, T. R. Naish, G. B. Dunbar, P. Stocchi, M. A. Kominz, P. J. J. Kamp, C. A. Tapia, R. M. McKay, R. H. Levy, M. O. Patterson, The amplitude and origin of sea-level variability during the Pliocene epoch. *Nature* **574**, 237–241 (2019).
53. M. A. Kominz, J. V. Browning, K. G. Miller, P. J. Sugarman, S. Mizintseva, C. R. Scotese, Late Cretaceous to Miocene sea-level estimates from the New Jersey and Delaware coastal plain coreholes: An error analysis. *Basin Res.* **20**, 211–226 (2008).
54. J. Jouzel, V. Masson-Delmotte, O. Cattani, G. Dreyfus, S. Falourd, G. Hoffmann, B. Minster, J. Nouet, J. M. Barnola, J. Chappellaz, H. Fischer, J. C. Gallet, S. Johnsen, M. Leuenberger, L. Loulergue, D. Luethi, H. Oerter, F. Parrenin, G. Raisbeck, D. Raynaud, A. Schilt, J. Schwander, E. Selmo, R. Souchez, R. Spahni, B. Stauffer, J. P. Steffensen, B. Stenni, T. F. Stocker, J. L. Tison, M. Werner, E. W. Wolff, Orbital and millennial Antarctic climate variability over the past 800,000 years. *Science* **317**, 793–796 (2007).
55. J. A. Higgins, A. V. Kurbatov, N. E. Spaulding, E. Brook, D. S. Introne, L. M. Chimiak, Y. Yan, P. A. Mayewski, M. L. Bender, Atmospheric composition 1 million years ago from blue ice in the Allan Hills, Antarctica. *Proc. Natl. Acad. Sci. U.S.A.* **112**, 6887–6891 (2015).
56. Y. Yan, M. L. Bender, E. J. Brook, H. M. Clifford, P. C. Kemeny, A. V. Kurbatov, S. Mackay, P. A. Mayewski, J. Ng, J. P. Severinghaus, J. A. Higgins, Two-million-year-old snapshots of atmospheric gases from Antarctic ice. *Nature* **574**, 663–666 (2019).
57. B. Bereiter, S. Shackleton, D. Baggenstos, K. Kawamura, J. Severinghaus, Mean global ocean temperatures during the last glacial transition. *Nature* **553**, 39–44 (2018).
58. H. L. Ford, M. E. Raymo, Regional and global signals in seawater $\delta^{18}O$ records across the mid-Pleistocene transition. *Geology* **48**, 113–117 (2019).
59. Y. M. Smith, D. J. Hill, A. M. Dolan, A. M. Haywood, H. J. Dowsett, B. Risebrobakken, Icebergs in the Nordic seas throughout the Late Pliocene. *Paleoceanogr. Paleoclimatol.* **33**, 318–335 (2018).
60. I. Bailey, G. M. Hole, G. L. Foster, P. A. Wilson, C. D. Storey, C. N. Trueman, M. E. Raymo, An alternative suggestion for the Pliocene onset of major northern hemisphere glaciation based on the geochemical provenance of North Atlantic Ocean ice-rafted debris. *Quat. Sci. Rev.* **75**, 181–194 (2013).
61. C. Ohneiser, F. Florindo, P. Stocchi, A. P. Roberts, R. M. DeConto, D. Pollard, Antarctic glacio-eustatic contributions to late Miocene Mediterranean desiccation and reflooding. *Nat. Commun.* **6**, 8765 (2015).
62. M. Mudelsee, T. Bickert, C. H. Lear, G. Lohmann, Cenozoic climate changes: A review based on time series analysis of marine benthic $\delta^{18}O$ records. *Rev. Geophys.* **52**, 333–374 (2014).
63. C. M. John, G. D. Karner, E. Browning, R. M. Leckie, Z. Mateo, B. Carson, C. Lowery, Timing and magnitude of Miocene eustasy derived from the mixed siliciclastic-carbonate stratigraphic record of the northeastern Australian margin. *Earth Planet. Sci. Lett.* **304**, 455–467 (2011).
64. A. J. P. Houben, C. A. van Mourik, A. Montanari, R. Coccioni, H. Brinkhuis, The Eocene–Oligocene transition: Changes in sea level, temperature or both? *Palaeogeogr. Palaeoclimatol. Palaeoecol.* **335–336**, 75–83 (2012).
65. M. A. Kominz, W. A. Van Sickel, K. G. Miller, J. V. Browning, Sea-level estimates for the latest 100 Million years: One-dimensional backstripping of onshore New Jersey boreholes, *22nd Annual Gulf Coast Section SEPM Foundation Bob F. Perkins Research Conference*, Houston, Texas, USA, 8 to 11 December 2002, pp. 303–315.
66. C. H. Lear, T. R. Bailey, P. N. Pearson, H. K. Coxall, Y. Rosenthal, Cooling and ice growth across the Eocene-Oligocene transition. *Geology* **36**, 251–254 (2008).
67. C. L. O'Brien, M. Huber, E. Thomas, M. Pagani, J. R. Super, L. E. Eldera, P. M. Hull, The enigma of Oligocene climate and global surface temperature evolution. *Proc. Natl. Acad. Sci. U.S.A.* **117**, 25302–25309 (2020).
68. R. M. McKay, P. J. Barrett, R. S. Levy, T. R. Naish, N. R. Golledge, A. Pyne, Antarctic Cenozoic climate history from sedimentary records: ANDRILL and beyond. *Phil. Trans. R. Soc. A* **374**, 20140301 (2016).
69. D. K. Hutchinson, H. K. Coxall, D. J. Lunt, M. Steinthorsdottir, A. M. DeBoer, M. Baatsen, A. von der Heydt, M. Huber, A. T. Kennedy-Asser, L. Kunzmann, J.-B. Ladant, C. H. Lear, K. Moraweck, P. N. Pearson, E. Piga, M. J. Pound, U. Salzmann, H. D. Scher, W. P. Sijp, K. K. Śliwińska, P. A. Wilson, Z. Zhang, The Eocene-Oligocene transition: A review of marine and terrestrial proxy data, models and model-data comparisons. *Clim. Past* **17**, 269–315 (2021).
70. S. Galeotti, R. DeConto, T. Naish, P. Stocchi, F. Florindo, M. Pagani, P. Barrett, S. M. Bohaty, L. Lanci, D. Pollard, S. Sandroni, F. M. Talarico, J. C. Zachos, Antarctic Ice Sheet variability across the Eocene-Oligocene boundary climate transition. *Science* **352**, 76–80 (2016).
71. H. D. Scher, S. M. Bohaty, J. C. Zachos, M. L. Delaney, Two-stepping into the icehouse: East Antarctic weathering during progressive ice-sheet expansion at the Eocene–Oligocene Transition. *Geology* **39**, 383–386 (2011).
72. P. U. Clark, D. Pollard, Origin of the middle Pleistocene transition by ice sheet erosion of regolith. *Paleoceanography* **13**, 1–9 (1998).
73. T. B. Chalk, M. P. Hain, G. L. Foster, E. J. Rohling, P. F. Sexton, M. P. S. Badger, S. G. Cherry, A. P. Hasenfratz, G. H. Haug, S. L. Jaccard, A. Martínez-García, H. Pälike, R. D. Pancost, P. A. Wilson, Causes of ice age intensification across the Mid-Pleistocene Transition. *Proc. Natl. Acad. Sci. U.S.A.* **114**, 13114–13119 (2017).
74. M. Willeit, A. Ganopolsky, R. Calov, V. Brovkin, Mid-Pleistocene transition in glacial cycles explained by declining CO_2 and regolith removal. *Sci. Adv.* **5**, eaav7337 (2019).
75. I. Bailey, C. T. Bolton, R. M. DeConto, D. Pollard, R. Schiebel, P. A. Wilson, A low threshold for North Atlantic ice rafting from "low-slung slippery" late Pliocene ice sheets. *Paleoceanography* **25**, PA1212 (2010).
76. M. Scheffer, J. Bascompte, W. A. Brock, V. Brovkin, S. R. Carpenter, V. Dakos, H. Held, E. H. van Nes, M. Rietkerk, G. Sugihara, Early-warning signals for critical transitions. *Nature* **461**, 53–59 (2009).
77. PALAEOSENS Project Members, Making sense of palaeoclimate sensitivity. *Nature* **491**, 683–691 (2012).
78. A. S. von der Heydt, P. Ashwin, C. D. Camp, M. Crucifix, H. A. Dijkstra, P. Ditlevsen, T. M. Lenton, Quantification and interpretation of the climate variability record. *Glob. Planet. Change* **197**, 103399 (2021).
79. R. E. Zeebe, L. J. Lourens, Solar System chaos and the Paleocene–Eocene boundary age constrained by geology and astronomy. *Science* **365**, 926–929 (2019).
80. H. K. Coxall, P. A. Wilson, H. Pälike, C. H. Lear, J. Backman, Rapid stepwise onset of Antarctic glaciation and deeper calcite compensation in the Pacific Ocean. *Nature* **433**, 53–57 (2005).
81. R. M. DeConto, D. Pollard, Rapid Cenozoic glaciation of Antarctica induced by declining atmospheric CO_2. *Nature* **421**, 245–249 (2003).
82. L. R. Kump, S. L. Brantley, M. A. Arthur, Chemical weathering, atmospheric CO_2, and climate. *Annu. Rev. Earth Planet. Sci.* **28**, 611–667 (2000).
83. E. Anagnostou, E. H. John, T. L. Babila, P. F. Sexton, A. Ridgwell, D. J. Lunt, P. N. Pearson, T. B. Chalk, R. D. Pancost, G. L. Foster, Proxy evidence for state-dependence of climate sensitivity in the Eocene greenhouse. *Nat. Commun.* **11**, 4436 (2020).
84. J. W. B. Rae, Y. G. Zhang, X. Liu, G. L. Foster, H. M. Stoll, R. D. M. Whiteford, Atmospheric CO_2 over the past 66 Million years from marine archives. *Annu. Rev. Earth Planet. Sci.* **49**, 599–631 (2021).
85. D. Lüthi, M. Le Floch, B. Bereiter, T. Blunier, J.-M. Barnola, U. Siegenthaler, D. Raynaud, J. Jouzel, H. Fischer, K. Kawamura, T. F. Stocker, High-resolution carbon dioxide concentration record 650,000-800,000 years before present. *Nature* **453**, 379–382 (2008).
86. S. C. Sherwood, M. J. Webb, J. D. Annan, K. C. Armour, P. M. Forster, J. C. Hargreaves, G. Hegerl, S. A. Klein, K. D. Marvel, E. J. Rohling, M. Watanabe, Z. T. Andrews, P. Braconnot, C. S. Bretherton, G. L. Foster, Z. Hausfather, A. S. von der Heydt, R. Knutti, T. Mauritsen, J. R. Norris, C. Proistosescu, M. Rugenstein, G. A. Schmidt, K. B. Tokarska, M. D. Zelinka, An assessment of Earth's climate sensitivity using multiple lines of evidence. *Rev. Geophys.* **58**, e2019RG000678 (2020).
87. M. Scheffer, S. R. Carpenter, T. M. Lenton, J. Bascompte, W. Brock, V. Dakos, J. van de Koppel, I. A. van de Leemput, S. A. Levin, E. H. van Nes, M. Pascual, J. Vandermeer, Anticipating critical transitions. *Science* **338**, 344–348 (2012).
88. R. Benzi, G. Parisi, A. Sutera, A. Vulpiani, Stochastic resonance in climatic change. *Tellus* **34**, 10–16 (1982).
89. D. Pollard, R. M. DeConto, A. A. Nyblade, Sensitivity of Cenozoic Antarctic ice sheet variations to geothermal heat flux. *Glob. Planet. Change* **49**, 63–74 (2005).
90. E. Gasson, R. M. DeConto, D. Pollard, R. H. Levy, Dynamic Antarctic ice sheet during the early to mid-Miocene. *Proc. Natl. Acad. Sci. U.S.A.* **113**, 3459–3464 (2016).
91. F. Colleoni, C. Wekerle, J.-O. Näslund, J. Brandefelt, S. Masina, Constraint on the penultimate glacial maximum Northern Hemisphere ice topography (≈140 kyrs BP). *Quat. Sci. Rev.* **137**, 97–112 (2016).

Acknowledgments

Funding: This study was supported by U.K. Natural Environment Research Council grant NE/P011381/1 (to G.L.F. and E.J.R.). This study also contributes to Australian Research

Council Discovery Project DP2000101157 (E.J.R., D.H., and G.L.F.). **Author contributions:** E.J.R. designed the project, developed the method, and led the write-up. All authors contributed to refining the method and validation, discussing results, and write-up. **Competing interests:** The authors declare that they have no competing interests. **Data and materials availability:** All data needed to evaluate the conclusions in the paper are presented in the paper and/or the Supplementary Materials and will be archived at both www.ncdc.noaa.gov/data-access/paleoclimatology-data/datasets/ and www.highstand.org/erohling/ejrhome.htm.

Submitted 2 November 2020
Accepted 12 May 2021
Published 25 June 2021
10.1126/sciadv.abf5326

Citation: E. J. Rohling, J. Yu, D. Heslop, G. L. Foster, B. Opdyke, A. P. Roberts, Sea level and deep-sea temperature reconstructions suggest quasi-stable states and critical transitions over the past 40 million years. *Sci. Adv.* **7**, eabf5326 (2021).

Science Advances

Sea level and deep-sea temperature reconstructions suggest quasi-stable states and critical transitions over the past 40 million years

Eelco J. Rohling, Jimin Yu, David Heslop, Gavin L. Foster, Bradley Opdyke and Andrew P. Roberts

Sci Adv **7** (26), eabf5326.
DOI: 10.1126/sciadv.abf5326